The Hopf-saddle-node bifurcation for fixed points of 3D-diffeomorphisms: a computer assisted dynamical inventory

Renato Vitolo*, Henk Broer†, Carles Simó‡

March 23, 2009

Abstract

Dynamical phenomena are studied near a Hopf-saddle-node (HSN) bifurcation of fixed points of 3D-diffeomorphisms. The interest lies in the neighbourhood of weak resonances of the complex conjugate eigenvalues and the $1:5$ case is considered here. A model map is obtained by a natural construction, through perturbation of the Poincaré-Takens vector field normal form. The model dynamics is systematically explored by computation of Lyapunov exponents and numerical continuation of quasi-periodic invariant circles and their bifurcations. For an invariant circle, the interaction of 1:5 resonance and quasi-periodic Hopf bifurcations is found to give rise to an intricate structure of secondary bifurcations of invariant circles and two-tori. This leads to a fractal-like pattern of quasi-periodic bifurcations. Global bifurcations arise in connection with a pair of saddle-focus fixed points: homoclinic tangencies appear near a sphere-like heteroclinic structure formed by the 2D stable and unstable manifolds of the saddle points. Strange attractors occur for nearby parameter values and two routes are described. One route involves a finite number of quasi-periodic period doublings of an invariant circle, followed by loss of reducibility. The other route involves intermittency due to a quasi-periodic saddle-node bifurcation of an invariant circle. By construction, the phenomenology of the model map is expected in generic families of 3D diffeomorphisms.

*School of Engineering, Computing and Mathematics, University of Exeter, Exeter, UK

†Dept. of Mathematics, University of Groningen, PO Box 800, 9700 AV Groningen, The Netherlands

‡Dept. de Matemàtica Aplicada i Anàlisi, Universitat de Barcelona, Gran Via 585, 08007 Barcelona, Spain

Contents

1 Introduction

In [18] the authors studied a model for the Hopf-saddle-node (HSN) bifurcation of fixed points of diffeomorphisms. By construction the model is 'as generic as possible' in the class of diffeomorphisms having a HSN bifurcation near a weak (1:5) resonance. Present purpose is to extend [18] focusing on:

1. interaction of resonances and quasi-periodic bifurcations;
2. homo- and heteroclinic bifurcations of saddle-focus fixed points.

Our working *Ansatz* is that the rich phenomenology of the model is expected in generic families of 3D diffeomorphisms. A potential application is the model in [16], describing the atmospheric baroclinic jet at midlatitudes in the Northern Hemisphere (implications for the phenomenon of low-frequency variability are discussed in [26]). The problem set-up is sketched in the next subsection. An overview of the model dynamics is given in Sec. 1.2, together with an outline of the paper.

1.1 Setting of the problem

The Hopf-saddle-node (HSN) bifurcation for fixed points of 3D diffeomorphisms occurs when the eigenvalues of the derivative are

$$e^{i\omega_0}, e^{-i\omega_0} \text{ and } 1, \tag{1}$$

subject to the non-resonance conditions

$$e^{in\omega_0} \neq 1 \text{ for } n = 1, 2, 3, 4, \tag{2}$$

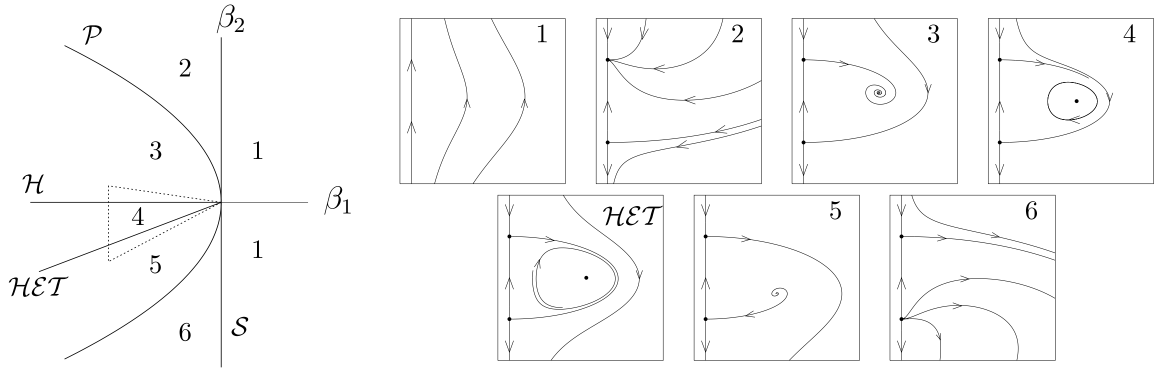

Figure 1: Bifurcation diagram and phase portraits of (6) for $s = 1$, $a_1 < 0$ [50, §8.5].

and to generic requirements on the higher-order terms and on the parameter dependence [18, Lemma 6]. In this paper we study the dynamics of the map

$$G : \begin{pmatrix} w \\ z \end{pmatrix} \mapsto \begin{pmatrix} e^{i(\omega_0+\gamma\delta)} w[1 - \gamma(\gamma\mu + az + \gamma z^2)] \\ z + \gamma(1 - |w|^2 - z^2) \end{pmatrix} + \begin{pmatrix} \gamma^3(\varepsilon_1 \overline{w}^4 + \varepsilon_2 z^4) \\ 0 \end{pmatrix}, \tag{3}$$

which is a model for the HSN bifurcation of fixed points. The family G depends on the real parameters (γ, μ, δ), and is given in the coordinates (w, z), where $w = x + iy \in \mathbb{C}$ and $z \in \mathbb{R}$. The constants $a = a_1 + ia_2 \in \mathbb{C}$, $\varepsilon_j \in \mathbb{R}$, $j = 1, 2$ belong to a fixed compact set. The parameter δ is a small detuning near the 1:5-resonant value $\omega_0 = 2\pi/5$.

The construction of G is only sketched here: see [18, 19] and [69, Sec. 4.1.2] for details. Starting point is a version of Takens's Theorem [63] stating that any HSN family of diffeomorphisms can be approximated by the time-one map of a HSN family of vector fields [18, Theorem 1]. The usual approximation procedure here is "reversed": model G is constructed by perturbing the flow of a 3D family of vector fields which is a normal form for the HSN bifurcation of equilibria. For vector fields, the eigenvalues at the central singularity in a HSN bifurcation are $\pm i\omega$ and 0. This linear part induces a formal axial symmetry [5, 24, 64], which, near the central singularity in the product of phase space and parameter space, allows a good approximation by the following family of axially symmetric vector fields:

$$Y_{\beta_1,\beta_2,\omega}(w, z) = \begin{pmatrix} (-\beta_2 + i\omega)w - awz - wz^2 \\ -\beta_1 - sw\overline{w} - z^2 \end{pmatrix}, \tag{4}$$

with $a = a(\beta_1, \beta_2, \omega) \in \mathbb{C}$, $s = \pm 1$ (see [50, Lemma 8.11] and [18, Lemma 6]). We choose the dynamically richest unfolding case $a_1 = \mathrm{Re}(a) < 0$ and $s = 1$, for which Hopf and heteroclinic bifurcations occur in (4). Restricting to $\beta_1 < 0$, the following transformation of time and variables is applied:

$$\beta_1 = -\gamma^2, \quad \beta_2 = \gamma^2 \mu, \quad t = \widehat{t}/\gamma, \quad w = \gamma \hat{w}, \quad z = \gamma \hat{z}. \tag{5}$$

The first term in (3) is obtained as an approximate time-γ map of the transformed vector field (hats are ignored for simplicity). The second term of (3) consists of perturbative terms of order four. By [18, Theorem 1], this construction contains a subclass of generic phenomena for HSN-diffeomorphisms.

We study the patterns for HSN diffeomorphisms which correspond to the Hopf and heteroclinic bifurcations of (4). In the chosen unfolding case, the 3D family $Y_{\beta_1,\beta_2,\omega}$ possesses a limit cycle $\mathscr{C}$, which loses stability at a Hopf-Neĭmark-Sacker [50] bifurcation[1] where an attracting two-torus $\mathscr{T}$ branches off. At a heteroclinic bifurcation, the

[1]For shortness and coherence with previous work [18, 19], this is called Hopf bifurcation henceforth.

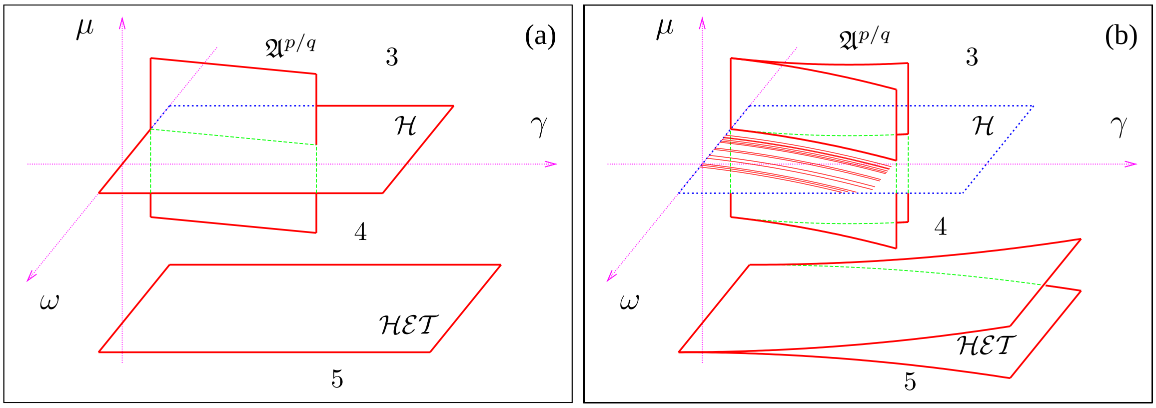

Figure 2: Sketch of the theoretical expectations for the bifurcation diagram of G (3) in the three-dimensional parameter space (γ, μ, ω). (a) Bifurcation set of the axially symmetric family of maps obtained for $\varepsilon_1 = \varepsilon_2 = 0$. The hypersurface $\mathfrak{A}^{p/q}$ consists of parameter values for which the rotation number on the invariant circle $\mathscr{C}$ is a fixed rational number $p/q \in \mathbb{Q}$. See the text for the meaning of $\mathcal{H}$ and $\mathcal{HET}$. (b) Expected bifurcation set of G (3) (assuming genericity). $\mathfrak{A}^{p/q}$ is a resonance wedge of rotation number p/q, $\mathcal{HET}$ is an exponentially narrow wedge where heteroclinic intersections and tangencies occur. Only a Cantor-like foliation by curves survives of the surface $\mathcal{H}$.

two-torus $\mathscr{T}$ merges into a sphere-like structure formed by the invariant manifolds of two saddle-focus equilibria $P_\pm$ belonging to the z-axis. Fig. 1 contains the bifurcation diagram and phase portraits of the planar reduction

$$\dot{r} = r(-\beta_2 - a_1 z - z^2), \quad \dot{z} = -\beta_1 - z^2 - sr^2, \tag{6}$$

obtained from (4) in cylindrical coordinates (r, ϕ, z), where $w = re^{i\phi}$ and the ϕ-component is disregarded. The Hopf and heteroclinic bifurcations of (6) are denoted as $\mathcal{H}$ and $\mathcal{HET}$, respectively, in Fig. 1. We refer to [18, 50] for details.

The qualitative sketch in Fig. 2, provided by the normal form, summarises our expectations for the bifurcation diagram of model map G and serves as reference in our study. Fig. 2 (b) is derived from Fig. 2 (a) using perturbation theory, normal hyperbolicity [35, 41] and quasi-periodic bifurcation theory [4, 7, 8, 32]. Consider the axially symmetric map obtained by setting $\varepsilon_j = 0$, $j = 1, 2$ in (3). When μ crosses zero (from region 3 to 4 in Fig. 2 (a)), a circle attractor with *parallel dynamics* (rigid rotation) loses stability and an invariant two-torus branches off. Due to the scaling (5), two saddle-focus fixed points $P_\pm$ are approximately located at the 'poles' $\approx (0, 0, \pm 1)$. For parameters on $\mathcal{HET}$ an invariant sphere is formed by the invariant manifolds of $P_\pm$. Three classes of dynamical phenomena are expected for G (Fig. 2 (b)):

1. Interaction of resonances and the Hopf-Neĭmark-Sacker bifurcation.

2. Two-torus breakdown near the heteroclinic region.

3. Two-torus dynamics and the Arnol′d resonance web.

Point 1: the Hopf-Neĭmark-Sacker bifurcation generically turns into a quasi-periodic Hopf bifurcation for maps [4, 7, 8, 32]. The circle attractors have a Diophantine rotation number for a (Whitney) smooth foliation of positive measure in parameter space, parametrised over a Cantor set. For parameters varying within this subset the circle attractors lose stability, whereby a (Diophantine) two-torus branches off. The domain of existence of invariant circles and two-tori can be extended by normal hyperbolicity, just leaving out 'bubbles' around all the weak resonance points on the Hopf surface $\mathcal{H}$. Intricate patterns of secondary bifurcations are expected inside the 'bubbles', where the invariant circle not always survives and transitions to chaotic dynamics are possible [2, 21, 29, 30, 31, 65, 70, 71]. The main point of interest is to understand the patterns of bifurcation near a 'bubble'. The 1:5 resonance, which has lowest order among those compatible with (2), is chosen because its effects on the bifurcation diagram are likely more visible than for higher order resonances.

Point 2: we study heteroclinic phenomena related to the invariant manifolds of the 'polar' saddles $P_{\pm}$. In the present case where we assume real analyticity, these phenomena are expected inside a wedge $\mathcal{HET}$ in parameter space which is exponentially narrow[2] as $\gamma \downarrow 0$ [11, 12, 13, 62]. Breakdown of two-tori occurs near the heteroclinic region, resulting in quasi-periodic Hénon-like [17, 20] and other types of strange attractors.

Point 3 has been the subject of a separate work [19] focusing on the organisation of resonant dynamics inside the two-torus attractor.

1.2 A roadmap in the parameter plane

We now give an overview of the dynamics of G: (μ, δ) are used as control parameters, whereas we fix $\gamma = 0.1$. $\varepsilon_1 = \varepsilon_2 = 1$, $a_1 = -1$, $a_2 = 1/\sqrt{2}$, $\omega_0/(2\pi) = 1/5$. These values allow to visualise most of the interesting phenomena and have been selected after preliminary explorations with several sets of values. Moderate variations of the chosen values do not affect the qualitative behaviour of G, whereas other choices can confine phenomena of interest to very small (μ, δ)-domains. The Lyapunov diagram in Fig. 3 shows the type of attractor of G as a function of (μ, δ). The diagram is obtained by scanning parameter values on a grid, decreasing μ along lines of constant δ. For each value of (μ, δ), the detected attractor is classified according to its Lyapunov exponents: see [18, 19, 61, 69] for the algorithm and Tab. 1 for the colour code. By (5), to decrease μ in Fig. 3 is roughly equivalent to decrease β_2 in Fig. 1:

1. first a quasi-periodic Hopf bifurcation is expected (denoted as $\mathcal{H}$ in Fig. 2 (b));
2. then a heteroclinic structure is expected, formed by the 2D manifolds $W^s(P_-)$ and $W^u(P_+)$ (region $\mathcal{HET}$ in Fig. 2 (b)).

These theoretical expectations are largely met. Model G has a circle attractor $\mathscr{C}$ for large μ, at the right part of Fig. 3. There the circle $\mathscr{C}$ is 1:5-resonant within the strip pointed by an arrow in Fig. 3. This strip will be denoted as the *1:5 resonance gap*: it corresponds to the tongue-shaped domain $\mathfrak{A}^{p/q}$ in Fig. 2 (b) (for $p/q = 1/5$). The circle $\mathscr{C}$ undergoes quasi-periodic Hopf bifurcations at a frayed boundary near $\mu = 0.98$. This corresponds to the Cantor-like boundary $\mathcal{H} \cap \{\gamma = 0.1\}$ in Fig. 2 (b) and will be denoted as $\mathcal{H}$ for simplicity. Our first point of interest is the interaction between the quasi-periodic Hopf bifurcation $\mathcal{H}$ and the 1:5 resonance gap (point 1 in the previous section). This part of the study is undertaken in Sec. 2.

A range of homo- and heteroclinic phenomena occur for smaller μ, near $\mathcal{HET} \cap \{\gamma = 0.1\}$ (for simplicity denoted as $\mathcal{HET}$):

1. the 2D manifolds $W^s(P_-)$ and $W^u(P_+)$ develop transversal heteroclinic intersections;

[2]To show this, a refined averaging technique might be used, which goes back on [53].

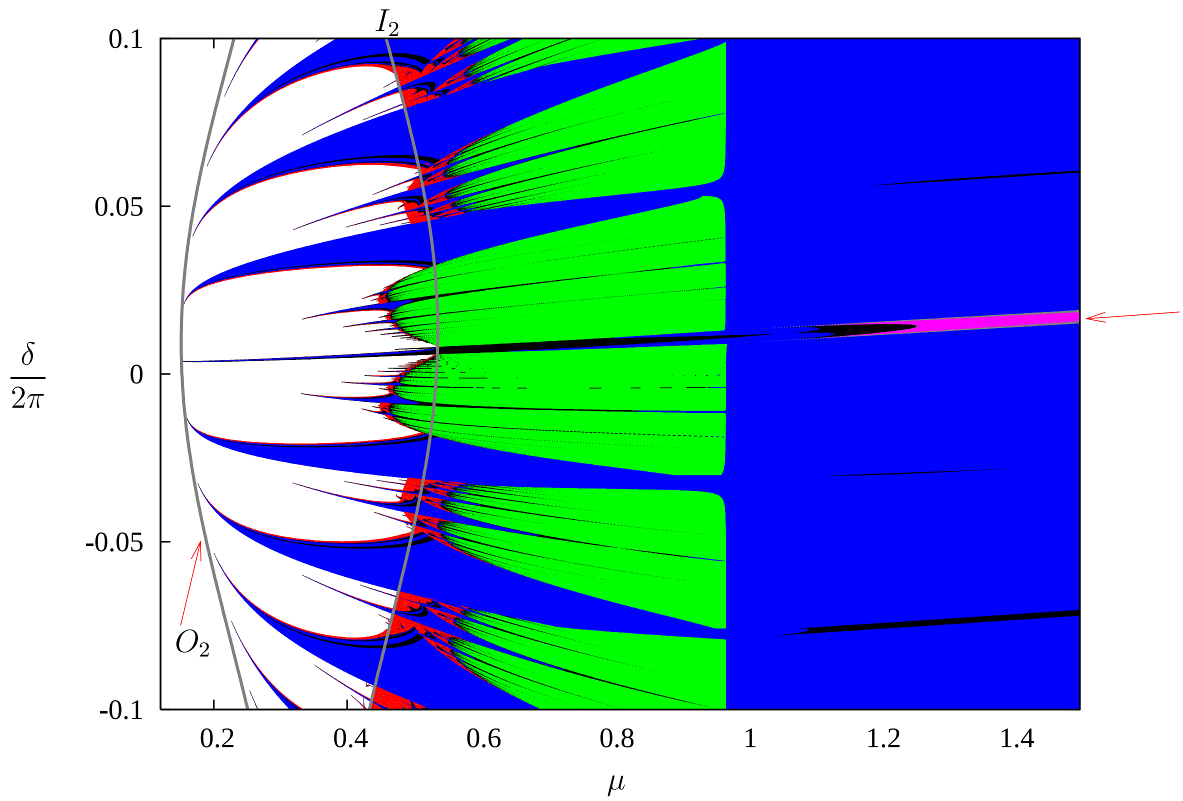

Figure 3: Lyapunov diagram of G in the $(\mu, \delta/(2\pi))$-parameter plane. The colours correspond to distinct classes of attractors, see Tab. 1. Yellow and pale blue pixels are almost absent. Grey regions are found near the boundary of the 1:5 resonance gap pointed to by an arrow. The two grey curves labelled I_2 and O_2 delimit the region $\mathcal{HET}$ characterised by homo- and heteroclinic intersections of the 'polar' fixed points $P_\pm$, see the text.

colour	Lyapunov exponents	attractor type
red	$\ell_1 > 0 = \ell_2 > \ell_3$	strange attractor
yellow	$\ell_1 > 0 > \ell_2 > \ell_3$	strange attractor
blue	$\ell_1 = 0 > \ell_2 = \ell_3$	invariant circle of focus type
green	$\ell_1 = \ell_2 = 0 > \ell_3$	invariant two-torus
black	$\ell_1 = 0 > \ell_2 > \ell_3$	invariant circle of node type
grey	$0 > \ell_1 > \ell_2 = \ell_3$	fixed point of focus type
fuchsia	$0 > \ell_1 = \ell_2 \geq \ell_3$	fixed point of focus type
pale blue	$0 > \ell_1 > \ell_2 > \ell_3$	fixed point of node type
white		no attractor detected

Table 1: Colour coding for the Lyapunov diagrams in Fig. 3, Fig. 7 (b), Fig. 19. The attractors of model map G (3) are classified by means of the Lyapunov exponents (ℓ_1, ℓ_2, ℓ_3).

2. the invariant manifolds $W^s(P_-)$ and $W^u(P_-)$ of the saddle-focus point P_- (located near the 'south pole') develop transversal homoclinic intersections;

3. similarly for the 'north pole' P_+.

The order in which these phenomena occur when μ is decreased varies with δ, giving rise to various configurations. The two curves I_2 and O_2 in Fig. 3 are 'inner' and 'outer' heteroclinic tangencies of the 2D manifolds $W^s(P_-)$ and $W^u(P_+)$. Strange attractors appear for nearby parameter values (red subregions). These phenomena (point 2 in the previous section) are analysed in Sec. 3. Open problems are summarised in Sec. 4.

2 The 1:5 resonance 'bubble'

The transition between a quasi-periodic invariant circle and a quasi-periodic two-torus may be direct or may involve a number of bifurcations, depending on the path we select in parameter space. If this path lies within the 1:5 resonance gap (pointed by an arrow in Fig. 3, see Sec. 1.2), Hopf bifurcations of periodic points occur, where periodically invariant circles are formed.[3] These circles undergo additional bifurcations, yielding complex bifurcation structures in the regions where the quasi-periodic Hopf boundary $\mathcal{H}$ intersects the 1:5 resonance gap. We call *the 1:5 'bubble'* a subset of the 1:5 resonance gap located near the intersection with $\mathcal{H}$ where the resonant invariant circle is destroyed by loss of normal hyperbolicity. A scenario involving bifurcations of periodic orbits is discussed in the next subsection. Secondary bifurcations of periodically invariant circles and two-tori are analysed in Sec. 2.2.

2.1 Destruction of the 1:5-resonant invariant circle

In this section we analyse the bifurcations of the invariant circle $\mathscr{C}$ within the 1:5 resonance gap and near the quasi-periodic Hopf bifurcation $\mathcal{H}$. The bifurcation diagram of period five points (Fig. 4 (a)) consists of:

- two curves $\mathcal{SN}^5_\pm$ of saddle-node bifurcations, which bound the 1:5 resonance gap (in red in Fig. 4 (a));

- an ellipse-shaped curve of Hopf bifurcations, split in two branches $\mathcal{H}^5_\pm$ by two HSN bifurcations $\mathcal{HSN}^5_\pm$ of period five points (in blue in Fig. 4 (a)). Here $\mathcal{SN}^5_\pm$ are tangent to $\mathcal{H}^5_\pm$.

Existence of this structure was analytically proved in [18]. The invariant circle $\mathscr{C}$ is normally hyperbolic for parameters sufficiently far from $\mathcal{H}$. Consider parameter values inside the 1:5 gap. For large μ, $\mathscr{C}$ is phase-locked: there exist two period five orbits P^5_- and P^5_+ such that $\mathscr{C} = P^5_- \cup W^u(P^5_+)$ (Fig. 5 (a)). Here P^5_- is an attracting node, P^5_+ a saddle-focus and $\mathscr{C}$ is attracting. For small μ, $\mathscr{C} = P^5_+ \cup W^u(P^5_-)$ is repelling: see Fig. 5 (b). Here P^5_+ is a repelling node and P^5_- a saddle-focus. The smoothness of the resonant circle $\mathscr{C}$ generically depends on its normal hyperbolicity: near the Hopf ellipse $\mathcal{H}^5_\pm$, $\mathscr{C}$ is generically expected to lose differentiability. The questions addressed here are:

1. In which subregions of the 1:5 resonance gap does $\mathscr{C}$ exist as a normally hyperbolic or as a continuous manifold?

[3] A periodically invariant circle is a set of curves $\{\mathscr{S}_j, j = 1, \ldots, p\}$, each of them homeomorphic to the unit circle, such that $G(\mathscr{S}_j) = \mathscr{S}_{j+1 \mod p}$. Therefore, $\mathscr{S}_j$ is an invariant circle for G^p.

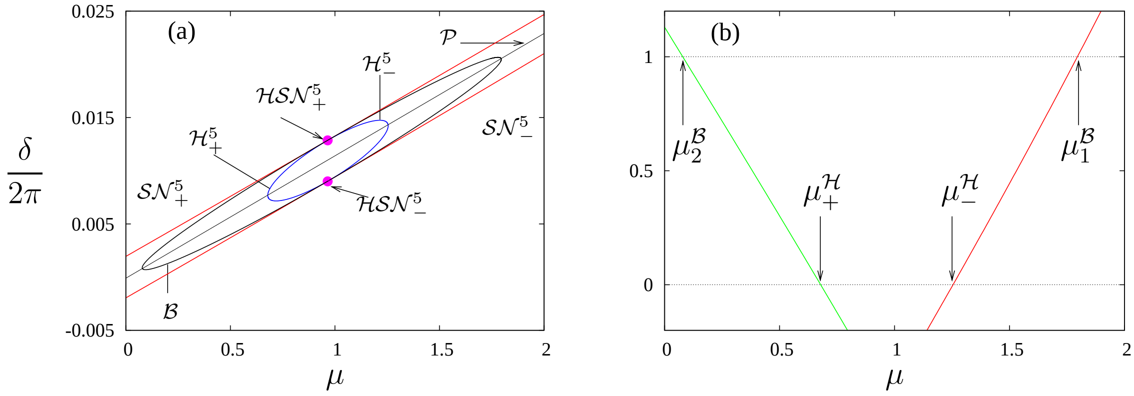

Figure 4: (a) The 1:5 resonance gap bounded by the saddle-node curves $\mathcal{SN}^5_\pm$ contains the "smoothness boundary" $\mathcal{B}$ and the Hopf ellipse $\mathcal{H}^5_\pm$. (b) Ratio of the absolute value of the Lyapunov exponents of the period five point P^5_- (red) and P^5_- (green) along the continuation path $\mathcal{P}$ (see text). The rightmost (leftmost) intersection between the path $\mathcal{P}$ and the smoothness boundary $\mathcal{B}$ is labelled as $\mu_1^{\mathcal{B}}$ ($\mu_2^{\mathcal{B}}$): for $\mu > \mu_1^{\mathcal{B}}$, normal contraction (represented by $\log|\lambda_c|$, which is negative) dominates tangential contraction (represented by $\log|\lambda_r|$), whereas for $\mu < \mu_2^{\mathcal{B}}$ normal expansion dominates tangential expansion. The location of the Hopf bifurcation for P^5_- (P^5_+) is labelled by $\mu_-^{\mathcal{H}}$ ($\mu_+^{\mathcal{H}}$).

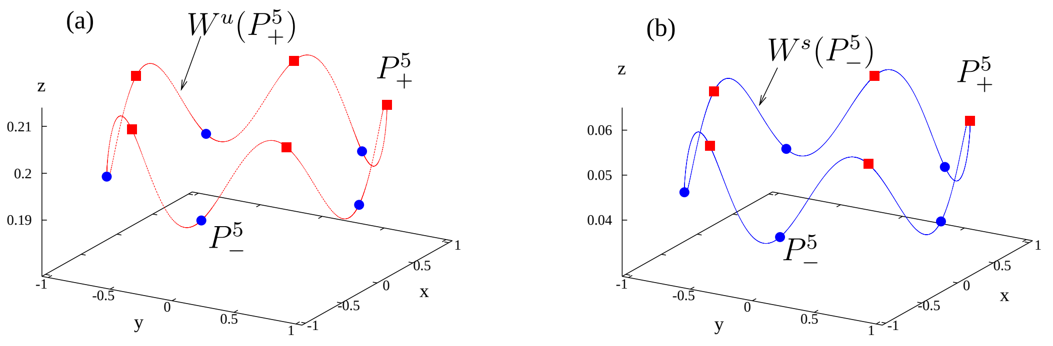

Figure 5: (a) The 1:5-resonant attracting invariant circle $\mathscr{C}$ is formed as the union of the unstable manifold $W^u(P^5_+)$ (red) with the node-focus attractor P^5_- (blue dots), where P^5_+ (red squares) is a saddle-focus. Parameters are outside the "smoothness boundary" $\mathcal{B}$ (see Fig. 4 (a)), at the right of the Hopf boundary $\mathcal{H}$. (b) The 1:5-resonant repelling circle $\mathscr{C}$ is formed by the union of the stable manifold $W^u(P^5_-)$ (blue) with the node-focus repellor P^5_+ (red squares), where P^5_- (blue dots) is a saddle-focus. Parameters are outside $\mathcal{B}$ and at the left of $\mathcal{H}$.

2. What kind of dynamics occurs when $\mathscr{C}$ does not persist?

The "smoothness boundary" $\mathcal{B}$ is a closed curve surrounding the Hopf ellipse in Fig. 4 (a). Within the 1:5 resonance gap, the circle $\mathscr{C}$ is normally hyperbolic for parameters outside the area enclosed by $\mathcal{B}$. The smoothness boundary is found by monitoring the eigenvalues of the derivative of the fifth iterate G^5 at the period five points $P^5_\pm$. The normal hyperbolicity of the phase-locked circle $\mathscr{C} = P^5_- \cup W^u(P^5_+)$ depends on the ratio $\log|\lambda_c|/\log|\lambda_r|$ (see [15, Secs. 3.1 and 5.3.1]). Here $\lambda_{r,c}$ are the eigenvalues of the derivative DG^5 at the attracting node P^5_-: DG^5 always has one real eigenvalue λ_r and a pair of complex conjugate eigenvalues $\lambda_c, \overline{\lambda}_c$, corresponding to Lyapunov exponents $\log|\lambda_r|$ (tangential contraction) and $\log|\lambda_c|$ (normal contraction), respectively. The right half of $\mathcal{B}$ is computed as the locus of parameter values for which $\log|\lambda_c|/\log|\lambda_r| = 1$. The left half of $\mathcal{B}$ is computed similarly, using the repelling node P_+ instead of P_-.

The ratio $\log|\lambda_c|/\log|\lambda_r|$ is plotted for both $P^5_\pm$ in Fig. 4 (b), for parameters along a path $\mathcal{P}$ located approximately halfway between the lines $\mathcal{SN}^5_\pm$ (see Fig. 4 (a)). The intersections of $\mathcal{P}$ with the smoothness boundary $\mathcal{B}$ are labelled as $\mu_1^{\mathcal{B}}$ and $\mu_2^{\mathcal{B}}$. For $\mu > \mu_1^{\mathcal{B}}$ normal attraction dominates tangential attraction at the node P_-, since $0 > \log|\lambda_r| > \log|\lambda_c|$. A phase portrait is given in Fig. 5 (a). Similarly, normal repulsion dominates tangential repulsion for $\mu < \mu_2^{\mathcal{B}}$ at the node P^5_+, see Fig. 5 (b) for a phase portrait.

Hopf bifurcations of period five points, belonging to the ellipse $\mathcal{H}^5_\pm$, are identified by a vanishing Lyapunov exponent. In Fig. 4 (b), P^5_- loses stability at $\mu_-^{\mathcal{H}}$, where a period five circle attractor $\mathscr{C}^5_-$ branches off. Similarly, P^5_+ undergoes a Hopf bifurcation belonging to $\mathcal{H}^5_+$ as μ decreases through $\mu_+^{\mathcal{H}}$, where a period five saddle-like invariant circle $\mathscr{C}^5_+$ is created. Bifurcations of $\mathscr{C}^5_\pm$ are examined in the next section.

For $\mu \in (\mu_-^{\mathcal{H}}, \mu_1^{\mathcal{B}})$ the circle $\mathscr{C}$ is not normally hyperbolic, since normal attraction is weaker than tangential attraction at the node P^5_-. However, the unstable manifold $W^u(P^5_+)$ is still attracted to P^5_-, thereby forming an invariant circle (a plot of this circle, not shown, looks like Fig. 5 (a)). Similarly, $\mathscr{C} = W^s(P^5_-) \cup \{P^5_+\}$ is not normally hyperbolic for $\mu \in (\mu_2^{\mathcal{B}}, \mu_+^{\mathcal{H}})$ (the corresponding plot looks like Fig. 5 (b)). We claim that this is C^0-persistence of $\mathscr{C}$ in the absence of normal hyperbolicity. In this case, $W^u(P^5_+)$ is generically expected to spiral around the 1D weak stable manifold of P^5_-, converging to P^5_- with a power law, see [15, Sec. 5.3.1]. Taylor expansions of order 50 have been used to compute $W^u(P^5_+)$ and the weak stable manifold $W^s(P^5_-)$ of the node P^5_- (see [60] for the algorithm). However, the generic power-law behaviour was not observed: the problem is that $W^u(P^5_+)$ and $W^s(P^5_-)$ are too close to be numerically distinguishable (with standard double precision), in the neighbourhood of P^5_- where the local approximation of $W^s(P^5_-)$ is sufficiently accurate. Such behaviour is found for other parameter values. This issue will be addressed in future research.

For parameters inside the Hopf ellipse $\mathcal{H}^5_\pm$, both $P^5_\pm$ are saddle-foci (with different stability types) and the circle $\mathscr{C}$ no longer exists. A configuration in phase space is illustrated in Fig. 6. The fifth iterate G^5 is used for ease of visualisation: only one 'fifth' of the whole portrait is shown. The unstable manifold $W^u(P^5_+)$ first approaches P^5_-, winding around the 1D stable manifold $W^s(P^5_-)$, see the magnification in the lower box of Fig. 6 (a). Then $W^u(P^5_+)$ flattens onto the two-dimensional unstable manifold $W^u(P^5_-)$ and spirals away from P^5_-. Lastly, $W^u(P^5_+)$ converges with 'scrolls' toward the period five circle $\mathscr{C}^5_-$ (upper box of Fig. 6 (a)): this is an attractor with normal behaviour of focus type. The 1D stable manifold $W^s(P^5_-)$ first approaches P^5_+ (box in Fig. 6 (b)), then winds away from it, escaping from the considered neighbourhood of the origin.

We now summarise our conclusions, based on the numerical evidence.

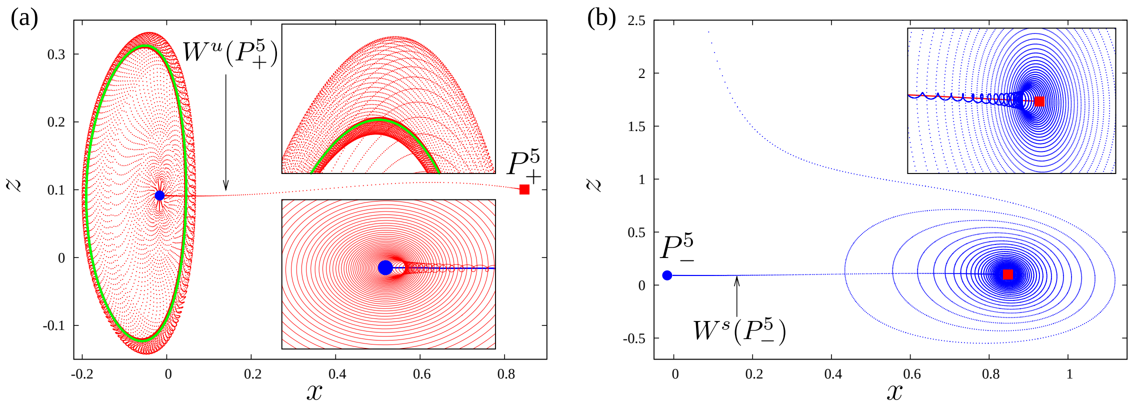

Figure 6: (a) Projection on (x,z) of the points P_-^5 (blue dot) and P_+^5 (red square), with one branch of the 1D unstable manifold $W^u(P_+^5)$ (red) and with the period five circle attractor $\mathscr{C}_-^5$ (green). Magnification of a neighbourhood of P_-^5 is given in the lower box, where a portion of $W^s(P_-^5)$ is added (blue). The upper box contains a magnification of the 'scrolls' of $W^u(P_+^5)$ around $\mathscr{C}_-^5$. (b) P_-^5 and P_+^5 are plotted together with one branch of $W^s(P_-^5)$ (blue). After approaching P_-^5 (in reversed time), $W^s(P_-^5)$ escapes to infinity. A neighbourhood of P_-^5 is magnified in the box, where a portion of $W^u(P_+^5)$ is included (red). Parameters are fixed at $(\mu, \delta/(2\pi)) = (1, 0.0097)$.

1. For parameters outside the smoothness boundary $\mathcal{B}$, the circle $\mathscr{C}$ persists as a smooth manifold, at least C^1.
2. For parameters in the annulus bounded between the smoothness boundary $\mathcal{B}$ and the Hopf ellipse $\mathcal{H}_\pm^5$, the circle $\mathscr{C}$ persists as a C^0 manifold. Or, at least, the lack of persistence is below the computer resolution (in present case the standard double precision).
3. Inside the Hopf ellipse the circle in general does not persist.

2.2 Bifurcation diagram

The analysis of the 1:5 bubble is now completed by examining bifurcations of invariant circles and two-tori. The bifurcation diagram (Fig. 7 (a) and Fig. 8) involves:

1. the curves $\mathcal{SN}_\pm^5$ and $\mathcal{H}_\pm^5$, tangent to each other at $\mathcal{HSN}_\pm^5$, see the previous section and compare with Fig. 4 (a).
2. Two degenerate Hopf bifurcations $\mathcal{DH}_\pm^5$ of period five points, belonging to $\mathcal{H}_+^5$.
3. Two 'curves' $\mathcal{HC}_\pm^5$ of quasi-periodic Hopf bifurcations of period five invariant circles ($\mathcal{HC}_+^5$ is not visible in Fig. 7 (a), since it is too close to $\mathcal{H}_\pm^5$, and it is not displayed in Fig. 8).
4. Two 'curves' $\mathcal{SNC}_\pm^5$ of quasi-periodic saddle-node bifurcations of a period five invariant circle.
5. Two 'curves' $\mathcal{SNT}_\pm$ of quasi-periodic saddle-node bifurcations of invariant two-tori (not displayed, since they are very close to $\mathcal{HC}_\pm^5$; $\mathcal{SNT}_-$ is shown in Fig. 8 (b)).
6. Two 'points' $\mathcal{BTC}_\pm^5$ where Bogdanov-Takens bifurcations of period five invariant circles take place.

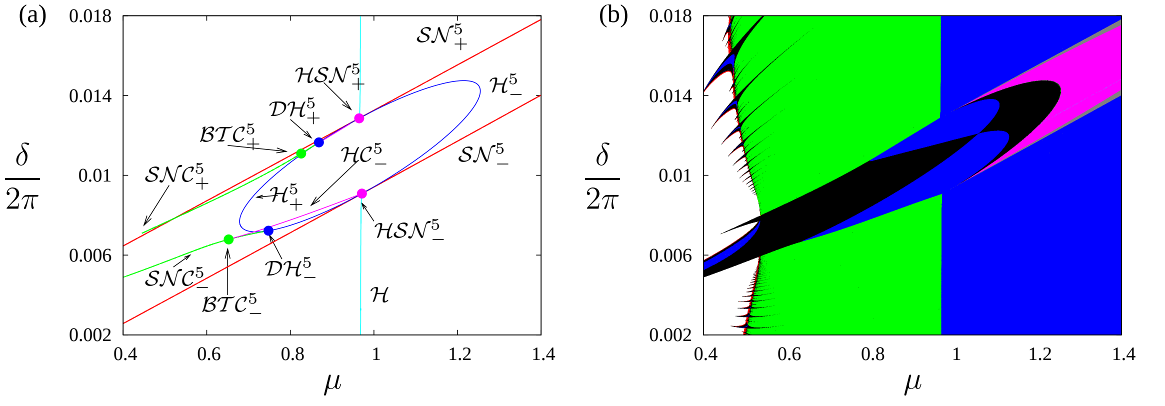

Figure 7: (a) Bifurcation diagram of G near the 1:5 'bubble', see the text for the notation. (b) Magnification of Fig. 3, same parameter window as in (a).

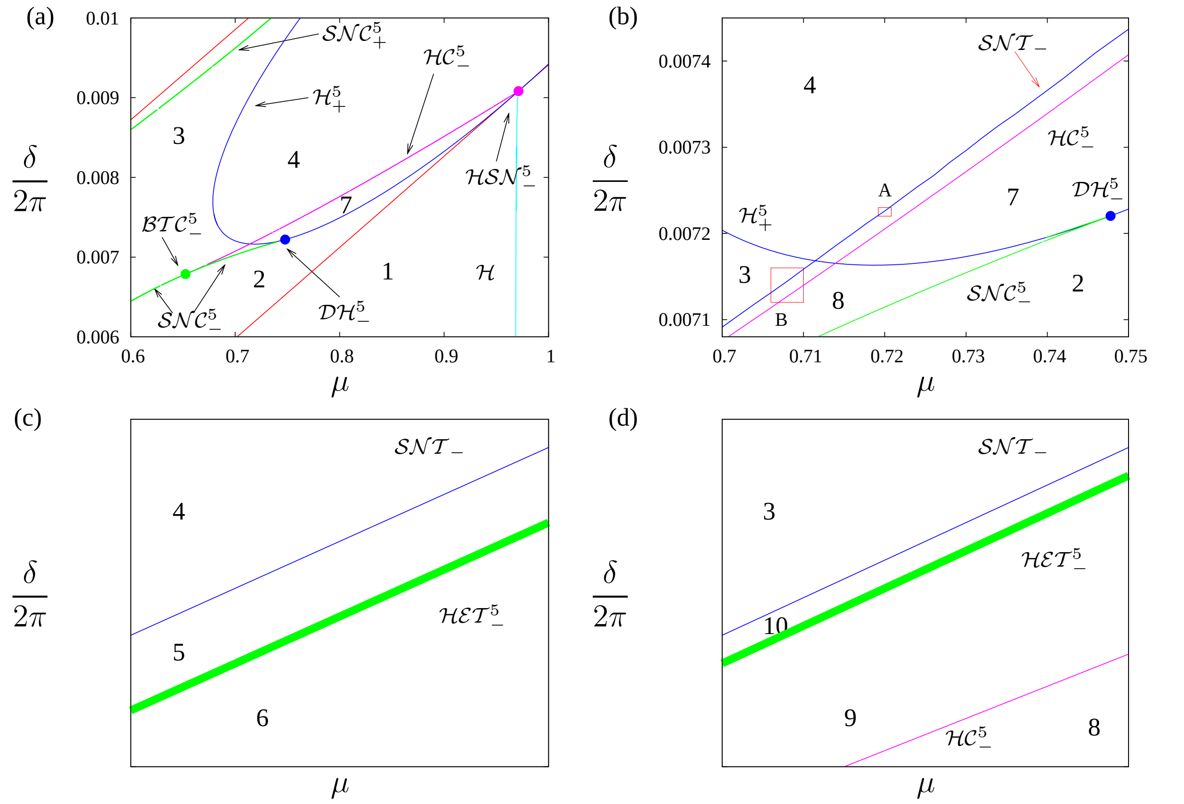

Figure 8: (a) Magnification of Fig. 7 (a) near the bifurcation 'curves' $\mathcal{HC}_\pm^5$ and $\mathcal{SNC}_\pm^5$. (b) Further magnification of (a). (c), (d) Qualitative sketches of the bifurcation diagram inside boxes labelled by A and B in (b), respectively.

Existence of $\mathcal{H}^5_\pm$, $\mathcal{SN}^5_\pm$ and $\mathcal{HSN}^5_\pm$ is proved in [19, 69]. The quasi-periodic bifurcations are computed by numerical continuation of invariant circles, performed by Fourier analysis [27, 28] (see [37, 51] for alternative methods). The normal behaviour is computed as in [43] for the bifurcation analysis, see the Appendix for details.

Remarks 1. 1. For quasi-periodic bifurcations, the word 'curves' is enclosed in quotes since the bifurcation sets are not smooth submanifolds of the parameter plane. The theoretical expectation for $\mathcal{SNC}^5_\pm$ and $\mathcal{HC}^5_\pm$ in Fig. 7 (a) is *the same* as for $\mathcal{H}$ (see Sec. 1.1): all these 'curves' are expected to be frayed Cantor-like boundaries interspersed of resonance bubbles. Resonance gaps are indeed numerically detected: most of them are tiny and the continuation algorithm can 'skip' them. However, the dynamical complexity described in [29, 30, 31] and in the present study is also expected at the 'bubbles' on the secondary quasi-periodic bifurcations. This implies that a cascade of subordinate quasi-periodic bifurcations takes place, corresponding to a fractal structure in parameter space.

2. Many bifurcation 'curves' in Fig. 7 (a) have a counterpart in the Lyapunov diagram in Fig. 7 (b). For example, $\mathcal{SNC}^5_+$ and $\mathcal{SNC}^5_-$ are the top and bottom boundary, respectively, between the black and green regions at the left of the Hopf boundary in Fig. 7 (b). Moreover, the 'curve' $\mathcal{SNT}_-$ is the lower boundary between green and blue regions, at the left of $\mathcal{H}$. Note that the transition from black to blue in Fig. 7 (b) is not a bifurcation: it is only a change of stability type of an invariant circle, from node to focus.

We now describe the lower branches $\mathcal{HC}^5_-$, $\mathcal{SNC}^5_-$, and $\mathcal{SNT}_-$ in the bifurcation diagram (the upper branches are organised similarly). The bifurcation diagram near degenerate Hopf bifurcations as $\mathcal{DH}^5_-$ is studied by Chenciner [29, 30, 31]: $\mathcal{DH}^5_-$ is the tangency point between the Hopf curve $\mathcal{HC}^5_-$ and the quasi-periodic saddle-node 'curve' $\mathcal{SNC}^5_-$. The bifurcation diagram near $\mathcal{BTC}^5_-$ has never been studied, to the best knowledge of the authors: $\mathcal{BTC}^5_-$ is a quasi-periodic Bogdanov-Takens bifurcations of periodically invariant circles. Both $\mathcal{SNC}^5_-$ and $\mathcal{HC}^5_-$ are frayed Cantor-like'curves' and the definition of their 'tangency' at $\mathcal{BTC}^5_-$ requires Whitney derivatives. Due to the density of resonances, two parameters are not sufficient to decide whether the tangency point $\mathcal{BTC}^5_-$ belongs to both Cantor-like 'curves' or falls within a resonance 'bubble'. By analogy with the Bogdanov-Takens bifurcation for fixed points [12, 13], homoclinic bifurcations are expected nearby. Further analysis will be carried out in future research.

The 'curve' $\mathcal{SNT}^5_-$ of quasi-periodic saddle-node bifurcations of invariant two-tori begins at the point $\mathcal{HSN}^5_-$ and terminates somewhere near $\mathcal{BTC}^5_-$. An approximation for $\mathcal{SNT}^5_-$ is here found by looking at attractors and repellors of G (3). Fourier methods [27, 28] might be used to compute it more accurately. However, a smooth parametrisation of a Diophantine family of invariant two-tori requires a parameter space of dimension at least three by dissipative KAM theory [4, 7, 8, 32]. The frequency vector of an invariant two-torus is Diophantine on a zero-dimensional subset of positive Lebesgue measure within the (μ, δ)-plane. An everywhere dense network of resonance gaps exists in the complement of the Diophantine set: the so-called *Arnol′d web* [19]. The ubiquitous Arnol′d web will cause numerical problems in a Fourier-based Newton algorithm: convergence requires spectral discretisation of very high order near resonances. This is particularly demanding for the computation of normal behaviour with the method of [43].

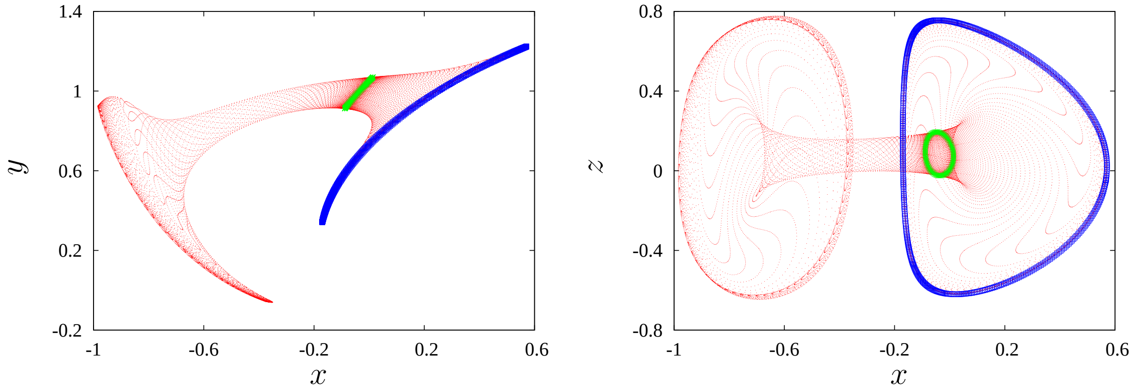

Figure 9: Projection on (x, y) (left) and on (x, z) (right) of the saddle-like period five invariant circle $\mathscr{C}_+^5$ (green) with both sides of $W^u(\mathscr{C}_+^5)$ (red) and with the period five circle attractor $\mathscr{C}_-^5$ (blue), for $(\mu, \delta/(2\pi)) = (0.746752823430779, 0.009760780820012)$ (in region 3 in Fig. 8 (a,b,d)). Only one 'fifth' of the whole two-torus is shown. Rotation numbers and eigenvalues are given in Tab. 2.

	ρ	$\lambda^{\parallel}$	$\lambda_1^{\perp}$	$\lambda_2^{\perp}$
$\mathscr{C}_+^5$	0.11109156678918	1.0	1.02186825875584	0.99929673737074
$\mathscr{C}_-^5$	0.08812166712298	1.0	0.98788853248803	0.95388810564241

Table 2: Rotation number ρ and eigenvalues of the period five invariant circles $\mathscr{C}_\pm^5$ in Fig. 9, see App. B for the notation and the algorithm. The fifth iterate G^5 is used for the numerical computations.

2.3 Transition sequences within the 1:5 bubble

Several parameter regions are identified in the bifurcation diagram in Fig. 8. We here discuss corresponding phenomena in phase space.

region 3: a phase-locked two-torus attractor $\mathscr{T}_- = \mathscr{C}_-^5 \cup W^u(\mathscr{C}_+^5)$ exists, see Fig. 9. Here $\mathscr{C}_-^5$ and $\mathscr{C}_+^5$ are period five invariant circles, the former being an attractor and the latter a saddle. The two-torus $\mathscr{T}_-$ bounds a volume containing the phase-locked circle $\mathscr{C}$, not shown (see Sec. 2.1). The smoothness of $\mathscr{T}_-$ depends on normal hyperbolicity at the node $\mathscr{C}_-^5$, compare with the discussion in Sec. 2.1.

From region 3 to 4: the circle $\mathscr{C}_+^5$ shrinks and collapses onto the period five point P_+^5 as the Hopf ellipse is approached 'from the outside'. The phase-locked two-torus of Fig. 9 becomes a 'trumpet' as in Fig. 6 (a) in region 4. Neither of $\mathscr{T}_-$, $\mathscr{C}_+^5$, or $\mathscr{C}$ exist here.

From region 3 to 2: $\mathscr{C}_\pm^5$ merge with each other and disappear through a quasi-periodic saddle-node bifurcation of period five invariant circles. Resonances interfere with this "annihilation" process in various ways [29, 30, 31]. The present novelty is that the saddle-node occurs inside the surface of a two-torus.

From region 4 to 5: a two-torus attractor $\mathscr{T}_-$ and a two-torus repellor $\mathscr{T}_+$ are created through a saddle-node bifurcation (same transition occurs from region 3 to 10). In region 5, $\mathscr{T}_+$ is contained in the volume bounded by $\mathscr{T}_-$; all the invariant manifolds of region 4 persist here and are contained in the volume bounded by $\mathscr{T}_+$ (Fig. 11 (a)).

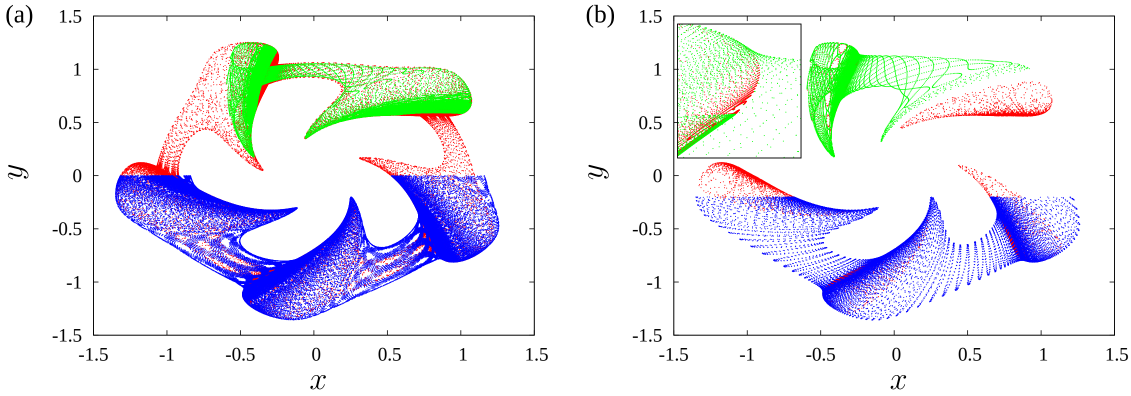

Figure 10: (a) Attracting two-torus $\mathscr{T}_-$ (blue), repelling two-torus $\mathscr{T}_+$ (red) with both sides of the unstable manifold of period five circle $\mathscr{C}^5_+$ (green), for $(\mu, \delta/(2\pi)) = (0.7081, 0.00714524)$ (in region 9 in Fig. 8 (d)). For $\mathscr{T}_-$, only points with $y < 0$ are shown. (b) Same as (a) for $(\mu, \delta/(2\pi)) = (0.7081, 0.007145585)$ (region 10), where the repelling period five two-torus $\mathscr{T}^5_+$ occurs (red). For $\mathscr{T}_-$, only points with $y < -0.2$ are shown.

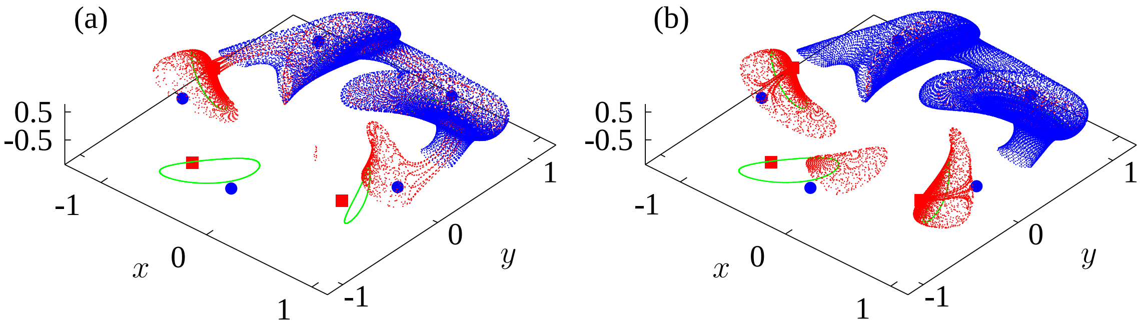

Figure 11: (a) Attracting two-torus $\mathscr{T}_-$ (blue), repelling two-torus $\mathscr{T}_+$ (red), period five circle attractor $\mathscr{C}^5_-$ (green), period five points P^5_- (thick blue dots) and P^5_+ (red squares), for $(\mu, \delta/(2\pi)) = (0.72, 0.00722673)$ (region 5 in Fig. 8 (c)). For $\mathscr{T}_-$ and $\mathscr{T}_+$, only points with $y > 0.2$ and $y > -0.3$, respectively, are shown. (b) Same as (a) for $(\mu, \delta/(2\pi)) = (0.72, 0.0072265)$ (region 6), where the repelling period five two-torus $\mathscr{T}^5_+$ occurs (red). For $\mathscr{T}_-$ and $\mathscr{T}^5_+$, only points with $y > 0.2$ and $y > -0.8$, respectively, are shown.

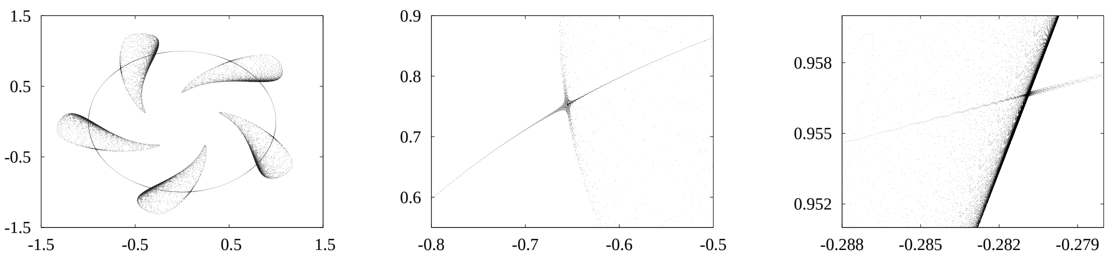

Figure 12: Left: projection on (x, y) of the repellor occurring at the transition between the configurations in Fig. 11, for $(\mu, \delta/(2\pi)) = (0.72, 0.0072266005)$. Centre, right: magnifications near the 'entrance' and 'exit' regions, respectively, of one of the five sphere-like components.

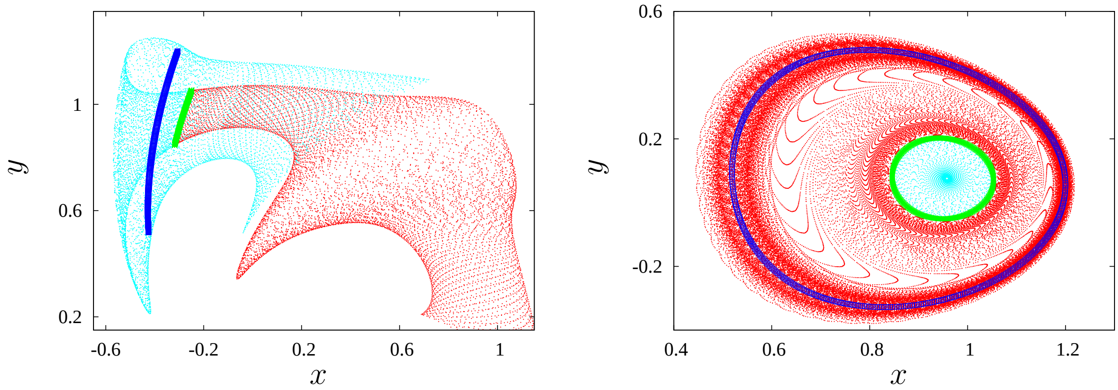

Figure 13: Left: projection on (x, y) of the saddle-like period five invariant circle $\mathscr{C}_+^5$ (green) and the circle repellor $\mathscr{C}_-^5$ (blue), with portions of the two branches of $W^u(\mathscr{C}_+^5)$ (red, pale blue). Right: projection on (y, z) of $W^s(\mathscr{C}_+^5)$: one branch (pale blue) is attracted in reversed time to the period five point repellor P_+^5, the other branch (red) converges to the circle repellor $\mathscr{C}_-^5$ (blue). Parameter values are $(\mu, \delta/(2\pi)) = (0.7081, 0.007127)$ (in region 8 in Fig. 8 (b,d)). Rotation numbers and eigenvalues of $\mathscr{C}_\pm^5$ are given in Tab. 3.

	ρ	$\lambda^{\parallel}$	$\lambda_1^{\perp}$	$\lambda_2^{\perp}$
$\mathscr{C}_+^5$	0.11114939770894	0.99999999999993	0.99964349714266	1.02531910506882
			$\lvert\lambda_1^{\perp}\rvert$	$\arg\lambda_1^{\perp}$
$\mathscr{C}_-^5$	0.10445033036985	0.99999999999994	1.00003133838885	0.00859935178207

Table 3: Top row: rotation number ρ and eigenvalues of the period five invariant circle $\mathscr{C}_+^5$ in Fig. 13. The three eigenvalues are real and $\mathscr{C}_+^5$ is of saddle type. Bottom row: same as top row for the repelling invariant circle $\mathscr{C}_-^5$, which is of focus type. The two normal eigenvalues $\lambda_{1,2}^{\perp}$ of $\mathscr{C}_-^5$ are complex conjugate: modulus and argument of $\lambda_1^{\perp}$ are displayed here in the third and fourth columns, respectively. The fifth iterate G^5 is used for numerical computations.

From 5 to 6: the two-torus repellor $\mathscr{T}_+$ approaches a heteroclinic structure formed by the transversal intersection of the 2D manifolds of the period five points $P_\pm^5$. Eventually $\mathscr{T}_+$ is destroyed: strange repellors as in Fig. 12 are found in the transition region $\mathcal{HET}_-^5$ (Fig. 8 (c)). Five repelling sphere-like heteroclinic structures exist in a normal form approximation near the secondary Hopf-saddle-node points $\mathcal{HSN}_\pm^5$ [69, Theorem 4.2]. These structures merge into one global repellor, connected by the 1D manifolds $W^s(P_-^5)$ and $W^u(P_+^5)$, since $\mathcal{HSN}_\pm^5$ take place on an invariant circle. This is the *reinjection* phenomenon of [48]. A period five two-torus repellor $\mathscr{T}_+^5$ shows up in region 6 (at the other side of the transition region), surrounding the circle attractor $\mathscr{C}_-^5$ (Fig. 11 (b)).

From region 6 to 7: the period five two-torus $\mathscr{T}_+^5$ collapses onto $\mathscr{C}_-^5$ at the bifurcation curve $\mathcal{H}_-^5$ (the same occurs from region 9 to 8). In region 7 $\mathscr{C}_-^5$ is repelling and the unstable manifold $W^u(P_+^5)$ is attracted to the two-torus $\mathscr{T}_-$, which surrounds everything.

region 8: The period five circles $\mathscr{C}_-^5$ (repellor) and $\mathscr{C}_+^5$ (saddle) coexist. One branch of $W^u(\mathscr{C}_+^5)$ first folds around $\mathscr{C}_-^5$, then wraps over the other branch of $W^u(\mathscr{C}_+^5)$ (Fig. 13 (a)). Both branches then converge to the two-torus attractor $\mathscr{T}_-$, which surrounds everything. One side of $W^s(\mathscr{C}_+^5)$ converges to the repellor $\mathscr{C}_-^5$, the other side to the repellor P_+^5 (Fig. 13 (b)).

region 10: $\mathscr{C}_-^5$ (attracting) and $\mathscr{C}_+^5$ (saddle) coexist and are contained in the volume bounded by a repelling two-torus $\mathscr{T}_-^5$. The latter is contained in the volume bounded by the attracting two-torus $\mathscr{T}_-$ (see Fig. 10 (a)). The unstable manifold $W^u(\mathscr{C}_+^5)$ converges with to $\mathscr{C}_-^5$ (which is of focus type) 'scrolling' around it: the union $W^u(\mathscr{C}_+^5) \cup \mathscr{C}_-^5$ forms a resonant, C^0, phase-locked invariant two-torus.

From region 10 to 9: the two-torus repellor $\mathscr{T}_+$ is destroyed by a homoclinic bifurcation, leading to the formation of a period five two-torus repellor $\mathscr{T}_+^5$ (Fig. 10 (b)). In region 5, $W^u(\mathscr{C}_+^5)$ converges to the period five circle attractor $\mathscr{C}_-^5$ and one branch of $W^s(\mathscr{C}_+^5)$ is attracted (in reversed time) to the two-torus repellor $\mathscr{T}_+$ (Fig. 10 (a)). In region 6, the relative positions of $W^s(\mathscr{C}_+^5)$ and $W^u(\mathscr{C}_+^5)$ are interchanged (Fig. 10 (b)): $W^u(\mathscr{C}_+^5)$ converges to the two-torus attractor $\mathscr{T}_-$ and one branch of $W^s(\mathscr{C}_+^5)$ is attracted (in reversed time) to $\mathscr{T}_+^5$. Therefore, there is a transition region $\mathcal{HET}_-^5$ (Fig. 8 (d)) where transversal homoclinic intersections of $W^s(\mathscr{C}_+^5)$ and $W^u(\mathscr{C}_+^5)$ take place.

region 9: A period five repelling two-torus $\mathscr{T}_+^5$ coexists with period five circles $\mathscr{C}_-^5$ (attracting) and $\mathscr{C}_+^5$ (saddle). Everything is contained in the volume bounded by the attracting two-torus $\mathscr{T}_-$ and $\mathscr{C}_-^5$ is contained inside the volume bounded by $\mathscr{T}_+^5$ (see Fig. 10 (b)).

The above analysis is necessarily schematic: a complete description is unfeasible due to the ubiquitous occurrence of resonances.

There are strong analogies between the bifurcation diagram presented above and that of a vector field on the cylinder constructed as a model for the homoclinic Hopf-saddle-node bifurcation of equilibria [48]. The semi-global bifurcation diagram in the neighbourhood of the point A_- in [48, Fig. 11] looks very similar to the bifurcation diagram near *both* points $\mathcal{HSN}_\pm^5$. We plan to investigate this relation in future research.

3 The heteroclinic region

We here examine the parameter region near the intersection of the wedge $\mathcal{HET}$ in Fig. 2 (b) with the plane $\{\gamma = 0.1\}$. Two classes of phenomena occur here:

1. homo- and heteroclinic bifurcations of the 'polar' fixed points;
2. breakdown of invariant two-tori and invariant circles, onset of strange attractors.

These are discussed in the next two subsection, respectively.

3.1 Homo- and heteroclinic tangencies of the saddle-focus fixed points

Consider the 3D vector field normal form in (4): at the bifurcation curve $\mathcal{HET}$ (Fig. 1), a sphere-like heteroclinic structure exists, formed by the union of the z-axis (which contains $W^u(P_-)$ and $W^s(P_+)$) with the 2D manifolds $W^s(P_-)$ and $W^u(P_+)$. Here $P_\pm$ are the saddle-focus fixed points located near the poles $(x, y, z) = (0, 0, \pm 1)$. The heteroclinic sphere splits into a transversal heteroclinic structure for generic families obtained by perturbing $Y_{\beta_1,\beta_2,\omega}$ [5, 22, 25, 45]. This allows the occurrence of Shil′nikov homoclinic bifurcations [5, 25, 36, 38, 50]. Understanding the dynamics of the model map G requires second perturbation step, this one within the class of diffeomorphisms. Additional complications arise here due to splitting of the manifolds at the tangencies. A Shil′nikov bifurcation for the vector field generically yields a wedge in parameter space for the diffeomorphism, characterised by transversal homoclinic intersections. Transversal heteroclinic intersections of the 1D manifolds are also possible. Although this phenomenon is not generic, it can be expected to have codimension 1 and, hence, to appear along lines in the (μ, δ) parameter space. However, no such line has been found in the domain shown in Fig. 3. This section aims to shed light on the organisation of homo/hetero-clinic phenomena for the map G.

Consider the relative positions of the 2D manifolds $W^s(P_-)$ and $W^u(P_+)$. To decrease μ for fixed (δ, γ) is roughly equivalent to decrease β_2 for fixed β_1 in Fig. 1. A perturbation argument based on phase portraits 4 and 5 in Fig. 1 suggests that $W^s(P_-)$ and $W^u(P_+)$ undergo the sequence of configurations sketched in the top row of Fig. 14 as μ is decreased. Numerical results fully match with this expectation. For parameters at the right of I_2 (see Fig. 3) $W^u(P_+)$ is enclosed in the volume bounded by $W^u(P_-)$: Fig. 14 bottom left shows the first intersections of $W^u(P_+)$ and $W^u(P_+)$ with the horizontal plane $\{z = 0\}$ for such parameter values. Here *first* means that we choose the intersection which is closest to P_+ or P_- in an adapted parametrisation (see App. A for details on the algorithm; note that $W^s(P_-)$ and $W^u(P_+)$ may fold back and have infinitely many intersections with $\{z = 0\}$). For parameters at the left of O_2 (see Fig. 3), the above situation is reversed (Fig. 14 bottom right). Transversal heteroclinic intersections occur for parameters between I_2 and O_2 (Fig. 14 bottom centre). By continuity, heteroclinic tangencies of $W^s(P_-)$ and $W^u(P_+)$ are expected for values of μ:

1. between the left and centre configurations in Fig. 14 (top row): these are denoted as 'inner' tangencies;

2. between the centre and right configurations in Fig. 14 (top row): these are called 'outer' tangencies.

Approximate locations of these 'inner' and 'outer' heteroclinic tangencies are identified by the grey curves labelled by I_2 and O_2 in Fig. 3. These curves are computed as zeroes of the minimum signed distance between the first 'equatorial' intersections of $W^u(P_+)$ and $W^s(P_-)$ with $\{z = 0\}$ (see App. A).

Remarks 2.

1. Generically, the point of heteroclinic tangency between $W^u(P_+)$ and $W^s(P_-)$ does not belong to the plane $\{z = 0\}$. Consequently, the curve I_2 is a *lower bound* for the location of the 'inner' heteroclinic tangencies. Indeed, 'equatorial tangencies' occurring on I_2 correspond generically to transversal heteroclinic intersections in 3D: this is observed by varying the 'height' of the horizontal intersection plane for $W^u(P_+)$ and $W^s(P_-)$. Similarly, the curve O_2 is an upper bound for the location of the 'outer' heteroclinic tangencies.

2. The intersections $W^s(P_-) \cap \{z = 0\}$ and $W^u(P_+) \cap \{z = 0\}$ are more 'pentagonal' for parameters near the 1:5 resonance gap (Fig. 14 bottom right). Farther from the gap they are 'rounder' (Fig. 14 bottom left). The signed radial distance between $W^s(P_-) \cap \{z = 0\}$ and $W^u(P_+) \cap \{z = 0\}$ is a function $sd(\theta)$ of the angular variable θ defining the radial direction (Fig. 15 (a)). For a fixed value of μ the distance $sd(\theta)$ oscillates with a larger amplitude near the 1:5 gap (Fig. 15 (b)). The distance between I_2 and O_2 is larger near the 1:5 gap because the 'inner' ('outer') tangency between $W^s(P_-) \cap \{z = 0\}$ and $W^u(P_+) \cap \{z = 0\}$ happens 'earlier' (respectively, 'later') as μ is decreased due to the wider oscillations of $sd(\theta)$.

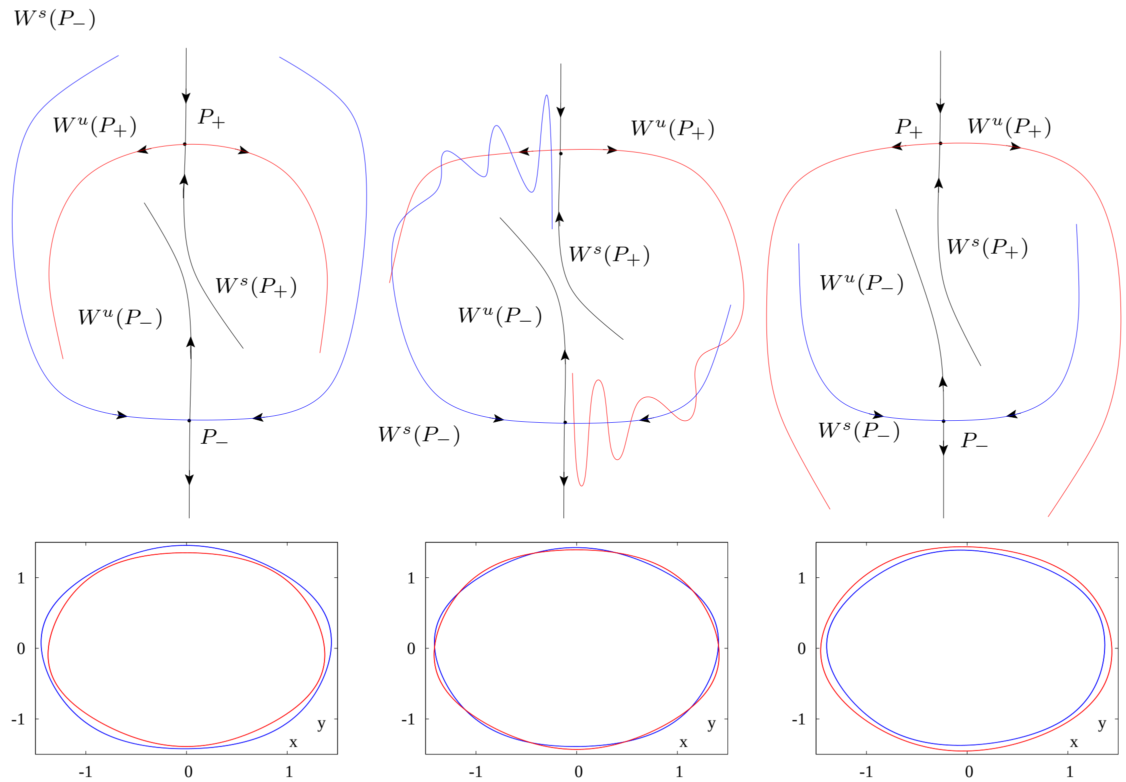

Figure 14: Top row: sketches of configurations for the invariant manifolds of the saddle-focus fixed points P_+ and P_- in region 5 (right), $\mathcal{HET}$ (centre), and 4 (left), where the notation for the regions refers to Fig. 2 (b), see text. The manifolds $W^s(P_-)$ (blue) and $W^u(P_+)$ (red) are in reality two-dimensional. Bottom row: intersection of $W^s(P_-)$ (blue) and $W^u(P_+)$ (red) with the $\{z = 0\}$-plane for the map G. From left to right, parameters are fixed at $(\mu, \delta/(2\pi)) = (0.6, 0)$, $(0.32, 0)$ and $(0, -0.1)$.

3. For large μ the 2D stable manifold $W^s(P_-)$ bounds an attracting invariant domain in phase space (Fig. 14 (a)). This domain is completely destroyed for small μ (Fig. 14 right). The Lyapunov diagram in Fig. 3 matches with this expectation: no attractor is detected at the left of curve O_2, whereas (at least) one attractor is found at the right of I_2. For intermediate parameter values, the existence of a transversal heteroclinic structure (Fig. 14 centre) implies that escape to $z \to -\infty$ is possible for certain (though not all) initial conditions: therefore, between I_2 and O_2 sometimes an attractor is detected in Fig. 3 and sometimes not.

We now turn to the transversal homoclinic intersections of the polar saddles. Consider first P_-: the upward branch of $W^u(P_-)$ first crosses the $\{z = 0\}$-plane and approaches P_+, then it starts spiraling away from P_+, closely following the 2D unstable manifold $W^u(P_+)$. Due to this closeness, the following sequence of configurations is expected as μ is decreased (by the same perturbation argument used above for the 2D manifolds based on phase portraits 4 and 5 in Fig. 1):

1. $W^u(P_-)$ remains inside the hemispheric 'cup' bounded by $W^s(P_-)$;

2. $W^u(P_-)$ has transversal homoclinic intersections with $W^s(P_-)$;

3. $W^u(P_-)$ lies completely outside the hemispheric cup and diverges to $z \to -\infty$.

Respective sketches are given in the top row of Fig. 16 (from left to right). Numerical simulations with map G confirm this expectation (Fig. 16 bottom row, from left to

(b)

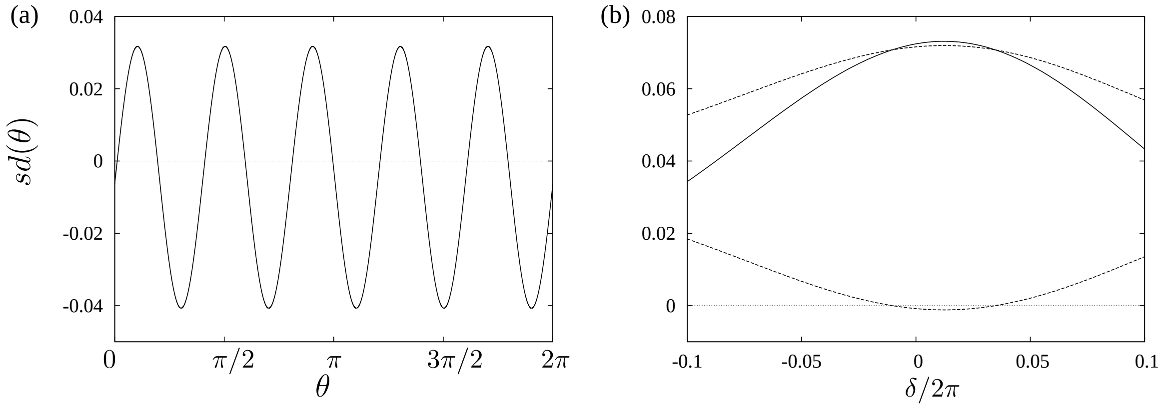

Figure 15: (a) Signed radial distance $sd(\theta)$ between the first 'equatorial' intersections $W^s(P_-) \cap \{z = 0\}$ and $W^u(P_+) \cap \{z = 0\}$ as a function of the angle θ defining the radial direction. Parameters $(\mu, \delta) = (0.32, 0)$ correspond to Fig. 14 bottom centre panel. (b) Amplitude (solid line), maximum and minimum (dashed lines) of the signed radial distance $sd(\theta)$ between $W^s(P_-) \cap \{z = 0\}$ and $W^u(P_+) \cap \{z = 0\}$ as a function of δ for $\mu = 0.53$. The amplitude is defined as $\max(sd(\theta)) - \min(sd(\theta))$. In an interval near $\delta = 0$ the minimum distance is negative: parameter values lie at the left of (and close to) curve I_2 in Fig. 3.

right). By continuity, homoclinic tangencies of $W^s(P_-)$ and $W^u(P_-)$ are expected for values of μ

1. between the left and centre configurations in Fig. 16 ('inner' tangencies);

2. between the centre and right configurations in Fig. 16 ('outer' tangencies).

Since these homoclinic tangencies are obtained by perturbation of Shil′nikov homoclinic bifurcations of a 3D vector field, we call them *Shil′nikov tangencies*. However, the concept of 'inner' and 'outer' tangencies is ambiguous in this case. If $W^u(P_-)$ is tangent to $W^s(P_-)$, then a piece of $W^u(P_-)$ near the first tangency point will approach $W^u(P_-)$ again after a number of iterates. Therefore, a portion of $W^u(P_-)$ will be mapped in a tubular neighbourhood of $W^u(P_-)$, near the first tangency point and after a number of iterates. This portion may intersect $W^s(P_-)$ transversally: therefore there must have been a 'previous' tangency between $W^u(P_-)$ and $W^s(P_-)$. For this reason, it might be impossible to define an 'inner' and 'outer' Shil′nikov homoclinic tangency (compare with [15]). What one can define unambiguously is the 'inner' and 'outer' tangency between the *first return* of $W^u(P_-)$ to a neighbourhood of P_-. As for the 2D manifolds, 'first' is understood as 'closest to P_- in an adapted parametrisation', see App. A.

The analysis of P_- is repeated, *mutatis mutandis*, for P_+. In reversed time (that is, using the inverse G^{-1}) the downward branch of $W^s(P_+)$ first crosses the plane $\{z = 0\}$ and approaches P_-, then it spirals away from P_-, closely following the 2D stable manifold $W^s(P_-)$. As μ is decreased, the expected sequence is now:

1. $W^s(P_+)$ remains inside the hemispheric 'cup' bounded by $W^u(P_+)$;

2. $W^s(P_+)$ has transversal homoclinic intersections with $W^u(P_+)$;

3. $W^s(P_+)$ lies completely outside the hemispheric cup and diverges to $z \to +\infty$.

Fig. 17 contains sketches (top row) and simulations with G (bottom row) confirming the above expectations. As above, continuity arguments suggests that homoclinic tangencies of $W^s(P_-)$ and $W^u(P_-)$ occur for values of μ

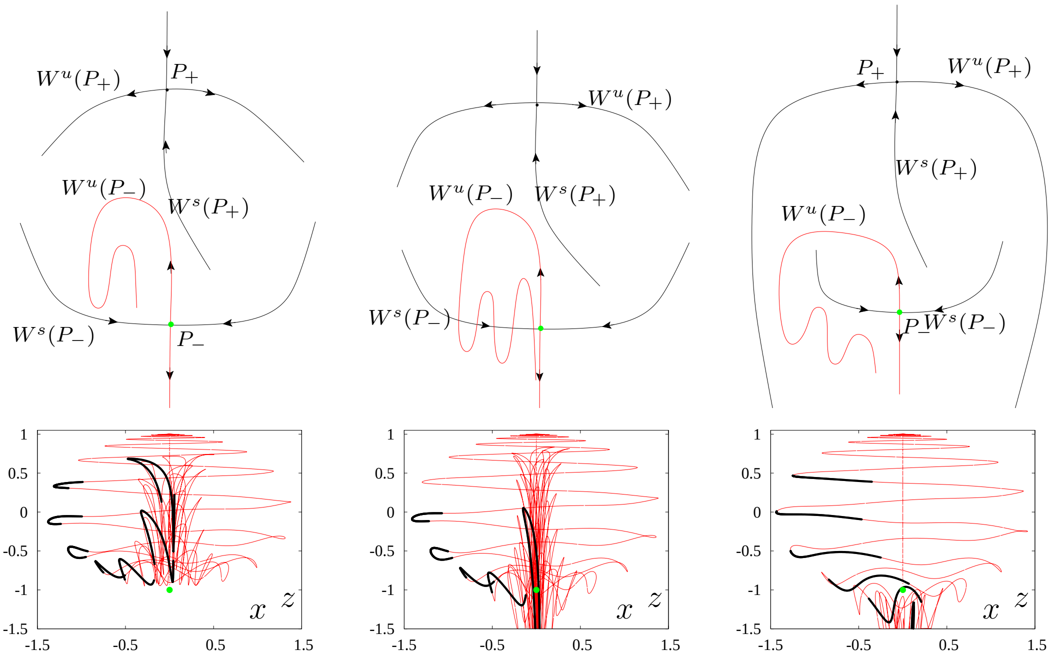

Figure 16: Top row: sketches of configurations for the invariant manifolds of the saddle-focus fixed point P_-. Note that, in fact, $W^u(P_-)$ goes up until it reaches points very close to P_+. Bottom row: numerical examples with map G of the sketches in the top row. The fixed point P_- (green dot) is plotted with part of the 1D manifold $W^u(P_-)$ (red). A few iterations of a fundamental domain (separated by 5 iterates or multiples of 5) are plotted with thicker black lines.

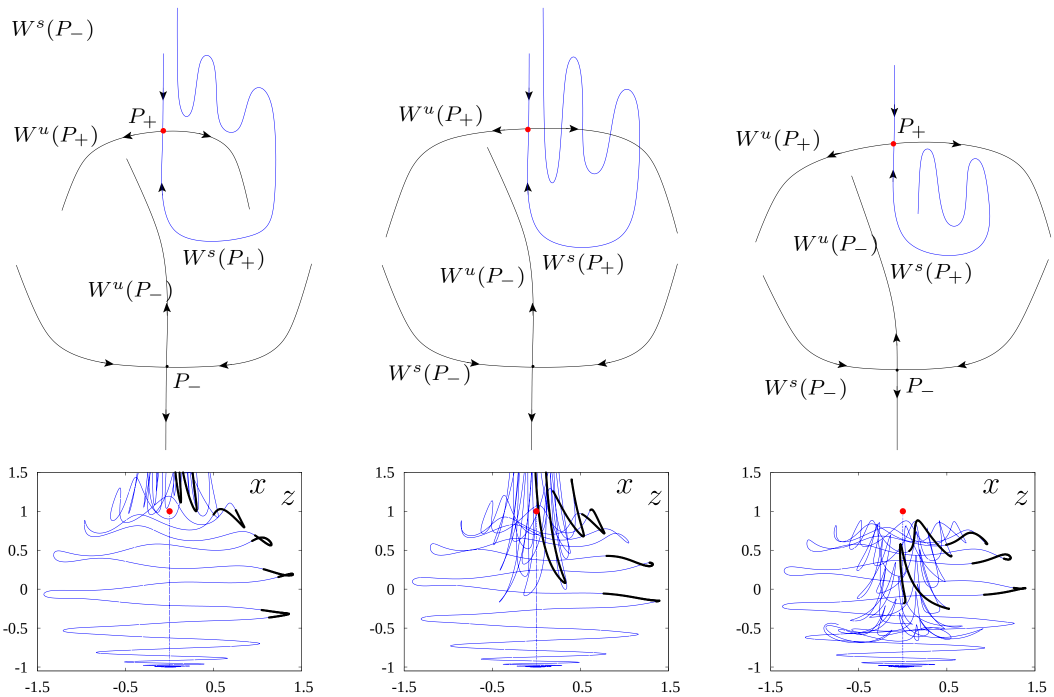

Figure 17: Same as Fig. 16 for the saddle-focus fixed point P_+. Note that, in fact, $W^s(P_+)$ goes down until it reaches points very close to P_-. Bottom row: numerical examples of the sketches in top row computed with map G. P_+ (red dot) is plotted with part of the 1D manifold $W^s(P_+)$ (blue) and a few iterations of a fundamental domain (separated by 5 or multiples of 5) are plotted with thicker black lines.

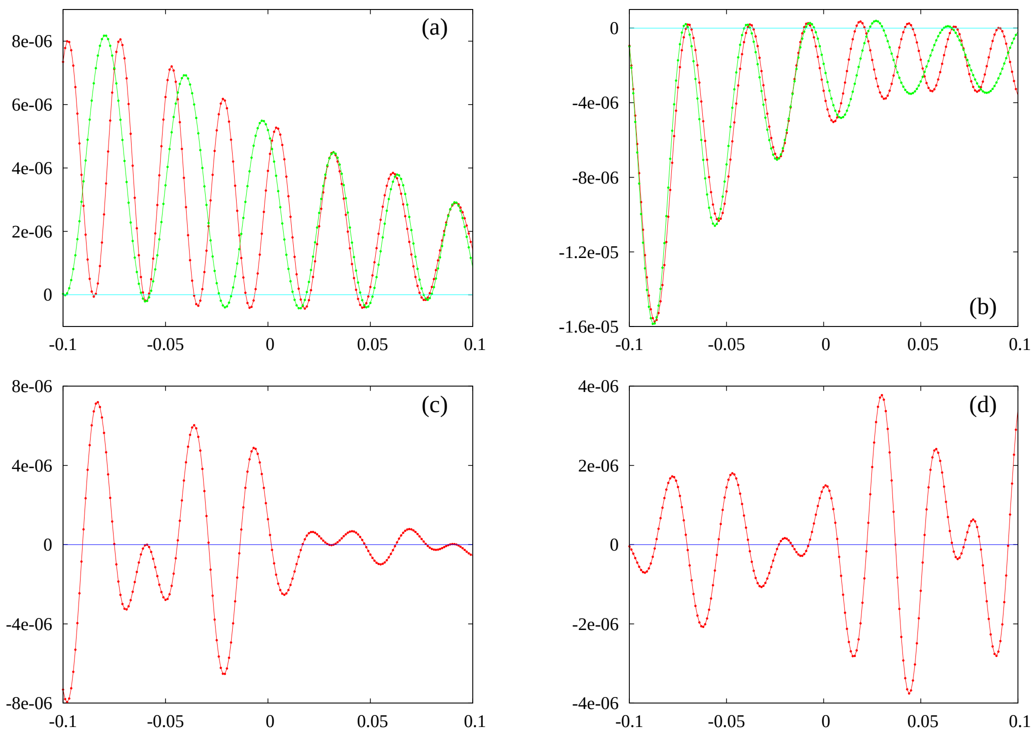

Figure 18: (a) Difference between the value of μ of the curves I_2 and I_{P_-} (O_{P_+}) as a function of δ, in red (green), see the text for details. (b) Same as (a) for O_2 and O_{P_-} (I_{P_+}), in red (green). (c) Difference between the value of μ of the curves I_{P_-} and O_{P_+}. (d) Same as (c) for O_{P_-} and I_{P_+}.

1. between the left and centre configurations in Fig. 16 ('inner' tangencies);

2. between the centre and right configurations in Fig. 16 ('outer' tangencies).

The last question which we address in this section is: what is the order in which the various tangencies occur as μ is decreased? We re-use the perturbation argument above, based on phase portraits 4 and 5 in Fig. 1. Since the upward branch of $W^u(P_-)$ eventually follows $W^u(P_+)$ very closely, it is expected that the 'inner' Shil′nikov tangency of P_- occurs very close (in parameter space) to the 'inner' heteroclinic tangency. Similarly, the 'outer' Shil′nikov tangency of P_+ is expected to occur nearby, due to the closeness between $W^s(P_-)$ and the downward branch of $W^s(P_+)$.

This expectation is confirmed: two curves I_{P_-} and O_{P_+} of are found very close to curve I_2 in the parameter plane. 'Inner' ('outer') Shil′nikov tangencies of P_- (P_+) occur for parameters on curve I_{P_-} (O_{P_+}), corresponding to the transition between the configurations in the left and centre panels in the bottom row of Fig. 16 (Fig. 17). Moreover:

1. the relative position of the Shil′nikov tangencies at curves I_{P_-} and O_{P_+} changes with δ, see Fig. 18 (c);

2. 'inner' Shil′nikov tangencies of $W^{u,s}(P_-)$ are impossible before (for μ decreasing) the 'inner' heteroclinic tangency: the two-dimensional manifold $W^u(P_+)$ is a separatrix which lies between the 1D manifold $W^u(P_-)$ and the 2D manifold $W^s(P_-)$, compare with Fig. 14 top left;

3. in principle, it is possible that the 'outer' Shil′nikov tangencies of P_+ occur before (for μ decreasing) the 'inner' heteroclinic tangency; this can only occur within the

small intervals where the difference of the μ-values of O_{P_+} and of I_2 is negative in Fig. 18 (b), compare with Remark 2.

Similar considerations hold near the 'outer' heteroclinic tangency (Fig. 18 (b,d)):

1. a curve I_{P_+} Shil′nikov 'inner' tangency of P_+ and a curve O_{P_-} of 'outer' tangency of P_- occur near O_2;

2. the relative positions of these Shil′nikov tangencies depends on δ (Fig. 18 (d));

3. 'inner' Shil′nikov tangencies of $W^{u,s}(P_+)$ are impossible after (for μ decreasing) the 'outer' heteroclinic tangency: there the 2D manifold $W^s(P_-)$ is a separatrix which lies between the 1D manifold $W^s(P_+)$ and the 2D manifold $W^u(P_+)$, compare with Fig. 14 top right.

4. in principle, it is possible that the 'outer' Shil′nikov tangencies of P_- occur after (for μ decreasing) the 'outer' heteroclinic tangency; this can only occur within the small intervals where the difference of the μ-values of O_{P_-} and of O_2 is positive in Fig. 18 (b), compare with Remark 2.

3.2 Strange attractors

Fig. 3 suggests that strange attractors of G are most abundant (from measure theoretic point of view in (μ, δ)-parameter plane) in region $\mathcal{HET}$. Two types of strange attractors may be distinguished on the basis of the Lyapunov exponents (ℓ_1, ℓ_2, ℓ_3):

$\ell_1 > 0$, $\ell_2 < 0$ (yellow): these will be called *Hénon-like*.

$\ell_1 > 0$, $\ell_2 \approx 0$ (red): these will be called *quasi-periodic Hénon-like*.

The second class is much more abundant than the first for G. Our terminology (Hénon-like versus quasi-periodic Hénon-like) is used for shortness: the detection of strange attractors based on Lyapunov exponents is not a proof of existence. Hénon-like attractors coincide with the closure of the 1D unstable manifold of a periodic orbit of saddle type [3, 52, 56, 66, 68] and possess one direction of instability [72], while the remaining directions are contracting. Quasi-periodic Hénon-like attractors coincide with the unstable manifold of a quasi-periodic invariant circle of saddle type [16, 17, 20, 69]. We expect the chaotic regions to be nowhere dense sets of positive measure, compare with [3, 52].

Several tongues occur in the parameter plane, at the left of the quasi-periodic Hopf boundary (Fig. 3). An attracting invariant circle exists for parameters inside a tongue: the circle is either of focus or node type (blue and black respectively, see Tab. 1). Most of the tongues widen up and eventually overlap as μ decreases (Fig. 19) yielding coexistence of different attracting invariant circles for the same parameter values. Coexistence of invariant circles and strange attractors has also been observed, but no coexistence of invariant two-tori and strange attractors seems to occur for G. Strange attractors of G often appear at the boundaries of the resonance tongues. We analyse two routes:

1. through the 'lateral' boundary of the resonance tongues; this involves a quasi-periodic saddle-node bifurcation of invariant circles where a phase-locked two-torus is destroyed;

2. through the 'left-end' boundary of the tongues; this involves a sequence of quasi-periodic period doublings of an invariant circle.

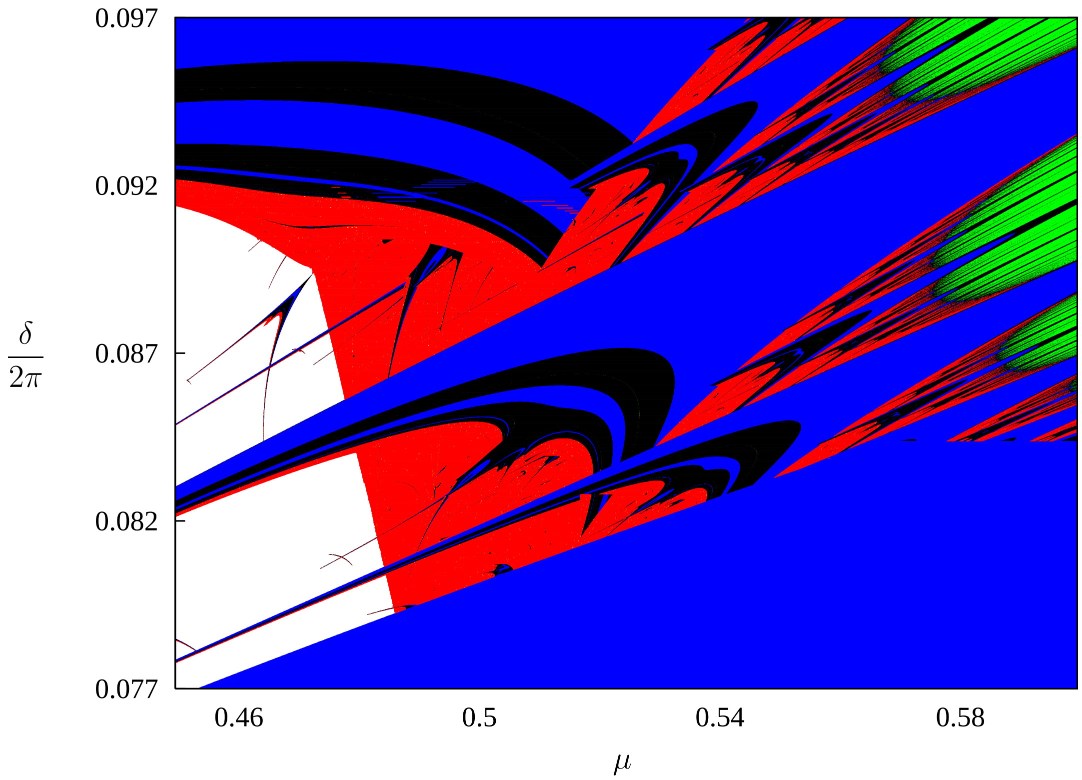

Figure 19: Lyapunov diagram of G in the $(\mu, \delta/(2\pi))$-plane. The attractors are classified by means of the Lyapunov exponents, coded according to Tab. 1.

These scenarios are described in the next two sections. Near the curve I_{P_-} (see the previous section), we would also expect the occurrence of Shil′nikov-like attractors for diffeomorphisms. However, all the strange attractors detected for G seem related to either of the two scenarios listed above and not directly to the Shil′nikov tangencies.

3.2.1 The quasi-periodic period doubling route

At the left-end of many resonance tongues in Fig. 19, there are alternating regions with an invariant circle of either focus (blue) or node type (black). This is due to the occurrence of several quasi-periodic period doublings of an invariant circle [7, 8]. This is a typical route for the creation of quasi-periodic strange attractors [16, 20, 67, 69]. This process starts from an attracting invariant circle $\mathscr{L}_0$ (Fig. 20 A), for parameters inside a resonance tongue. Five consecutive quasi-periodic period doublings take place as μ is decreased. 'Doubled' attracting circles $\mathscr{L}_1, \ldots, \mathscr{L}_5$ are created: $\mathscr{L}_i$ is attracting in a parameter interval $\mu_{i+1} < \mu < \mu_i$; Fig. 20 B contains a plot of $\mathscr{L}_2$. These bifurcations are of 'length doubling' type: the 'doubled' circle attractor created at each bifurcation is one connected closed curve and its length is roughly twice the length of the invariant circle which has lost stability [8, 25, 38].

A strange attractor replaces $\mathscr{L}_5$ by decreasing μ (Fig. 20 C). This strange attractor is formed by one narrow band, closely winding around the phase-space region previously occupied by $\mathscr{L}_5$. The various parts of the band merge together as μ decreases (Fig. 20 D). A similar band-merging process has been described for the Hénon-Pomeau attractor in [59]. The similarity is made clear by examining intersections of the attractors with horizontal planes. The circle attractor in Fig. 20 (A) intersects the plane $z = 0$ at 10 points (5 'outer' and 5 'inner' points). The rightmost 'outer' intersection point is

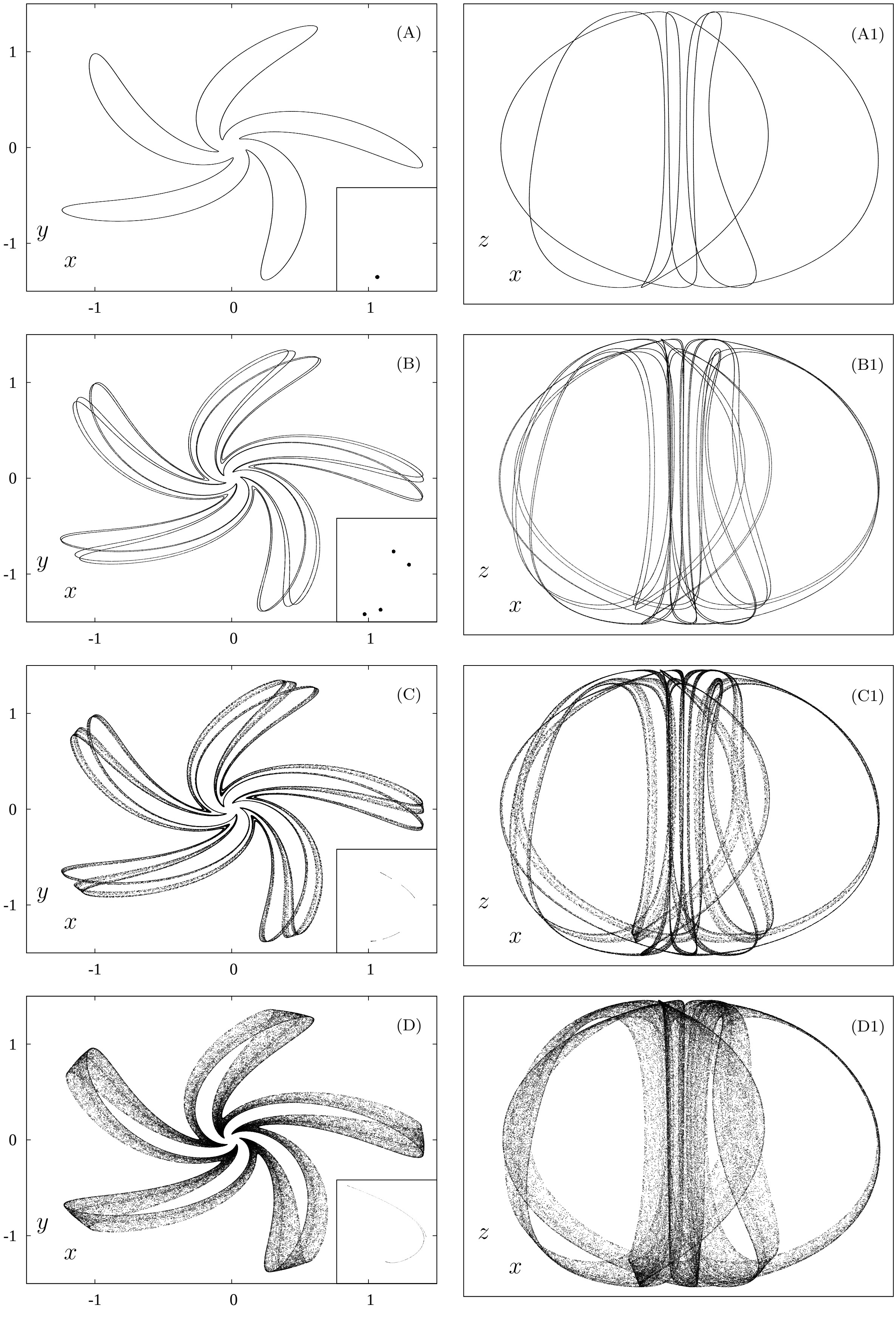

Figure 20: Attractors of the model map G (3) for $\delta/(2\pi) = 0.0324$ fixed, and for four values of μ. Projections on (x, y)-plane, where $w = x + iy$ (left column) and on (x, z) (right column). (A) $\mu = 0.53$, (B) 0.49, (C) 0.48, (D) 0.46, see Tab. 4 for the Lyapunov exponents and Tab. 5 for the rotation numbers. The small boxes in the left column display 'slices' of the attractors by a layer of width $2 \cdot 10^{-5}$ around the plane $z = 0$, in the window $(x, y) \in [1.382, 1.408] \times [-0.25, 0.17]$.

shown in the box of Fig. 20 (A) (approximations for the intersections are obtained by 'slicing' the attractors, that is selecting points that fall within thin horizontal layers). The circle attractor in Fig. 20 (B) intersects the plane $z = 0$ at 40 points (20 'outer' and 20 'inner' points). The rightmost 'outer' group of 4 points is shown in the box of Fig. 20 (B). A slice of the strange attractor Fig. 20 (C) contains four bands: these merge into a single band for the attractor in Fig. 20 (D), see the respective boxes. The second Lyapunov exponent of the strange attractors in Fig. 20 (C) and (D) equals zero (within the achieved numerical precision), see Tab. 4. All the above suggests that these strange attractors are of quasi-periodic Hénon-like type [20]. In particular, the single-band attractor in Fig. 20 (D) might coincide with the closure of $W^u(\mathscr{L}_5)$. We plan to investigate this possibility in simpler models, such as that of [17].

Do *finitely* or *infinitely* many quasi-periodic doublings take place? We believe that finitely many doublings lead to the creation of a strange attractor and propose the following explanation. At some moment in the finite cascade, the doubled attracting invariant circle loses reducibility between two consecutive doublings. The parameter sets characterised by lack of reducibility become increasingly wider at subsequent doublings. Then a strange attractor is formed at once, when a doubling occurs for a non-reducible attracting circle. This theoretical scenario is based on [39, 40], where a linear version of the problem is studied and on [44], where a 1D example is worked out, also see [14] for examples of the effect of the lack of reducibility in linear problems. Existence of a strange attractor is conjectural here as well as in the above papers.

The above scenario is suggested by analysis of the Lyapunov exponents $\ell_1 \geq \ell_2 \geq \ell_3$ as a function of μ with fixed δ (Fig. 21). Quasi-periodic period doublings occur whenever ℓ_2 vanishes (labelled 1–5). By decreasing μ across μ_1, $\mathscr{L}_0$ loses stability and the doubled attractor $\mathscr{L}_1$ is formed, which is reducible with real eigenvalues (both normal eigenvalues are positive and less than 1). One of the eigenvalues corresponding to the normal directions to $\mathscr{L}_2$ crosses -1 at μ_2, across a quasi-periodic period doubling. There is an interval of μ between μ_1 and μ_2 where the two normal eigenvalues collide, leaving the positive real axis into the complex plane (this is where $\ell_2 = \ell_3$), then race around the origin and collide again on the negative real axis. This process is typical for periodic points of diffeomorphisms and is described in *e.g.* [15, Fig. 12]. For this to be possible in the present case, the invariant circles must be reducible [43]. However, for smaller μ the above process no longer occurs: $\mathscr{L}_3$ and $\mathscr{L}_4$ never become of focus type. As μ is decreased, $\mathscr{L}_3$ crosses a parameter region N_1 where it ceases to be reducible: at the right of N_1, $\mathscr{L}_3$ is reducible and the eigenvalues are real and positive, whereas at the left the eigenvalues are real and negative (Fig. 21 centre). The same happens for $\mathscr{L}_4$ and $\mathscr{L}_5$. We conjecture that $\mathscr{L}_5$ is destroyed when it undergoes a non-reducible quasi-periodic doubling, where the second Lyapunov exponent vanishes (Fig. 21 right).

3.2.2 The intermittency route

The 'lateral' boundaries of the resonance tongues in Fig. 19 consist of quasi-periodic saddle-node bifurcations of invariant circles: there, again, we expect the dynamical complexity described in [29, 30, 31]. It may happen that the resonant two-torus is destroyed inside the resonance tongue by a homo- or heteroclinic tangency, compare with [15] for similar scenarios. If the circle attractor then disappears through a quasi-periodic saddle-node bifurcation, an intermittent transition to chaos takes place. Consider the two-torus attractor $\mathscr{T}_-$ in Fig. 22 A. When μ is decreased, $\mathscr{T}_-$ approaches a resonance tongue. Intermittent dynamics occurs on $\mathscr{T}_-$ near the tongue boundary (Fig. 22 B). Right after the saddle-node, the two-torus attractor $\mathscr{T}_-$ is phase-locked: $\mathscr{T}_- = \mathscr{L}_- \cup W^u(\mathscr{L}_+)$, where $\mathscr{L}_-$ is an attracting invariant circle and $\mathscr{L}_+$ is a saddle (Fig. 22 C). This is the

	ℓ_1	ℓ_2	ℓ_3	D_L
A	0.00000013	-0.00047684	-0.02295081	1.0003
B	0.00000000	-0.00700968	-0.01516126	1.0000
C	0.00130452	0.00000006	-0.02316217	2.0563
D	0.00403507	-0.00000018	-0.02529488	2.1595

Table 4: Lyapunov exponents ℓ_j and dimension D_L of the attractors in Fig. 20, computed using 10^7 iterates of the derivative.

	ρ_1	σ_{ρ_1}	ρ_2	σ_{ρ_2}	ρ	σ_ρ
A	0.077626693	3.9e-10	-0.388133466	3.0e-10	-0.128433623	6.4e-10
B	0.078507085	7.8e-10	-0.392535425	7.0e-10	-0.131635645	8.7e-10
C	0.078755714	3.2e-09	-0.39377857	2.4e-08	-0.133333333	4.7e-10
D	0.0792556	8.8e-07	-0.396278	4.4e-06	-0.135237	7.3e-06

Table 5: Rotation numbers ρ_j and uncertainties σ_{ρ_j}, for $j = 1, 2$, together with ratio $\rho = \rho_1/\rho_2$ and related uncertainty $\sigma_\rho = \rho_2\sigma_{\rho_1} + \rho_1\sigma_{\rho_2} + \sigma_{\rho_1}\sigma_{\rho_2}$, for the attractors in Fig. 20, computed using 10^6 iterates of G along an orbit.

	ℓ_1	ℓ_2	ℓ_3	D_L
A	0.00000019	0.00000015	-0.01644002	2.0000
B	0.00000033	-0.00000017	-0.01727034	2.0000
C	0.00000008	-0.00879667	-0.00879696	1.0000
D	0.00106329	0.00000008	-0.01900119	2.0560

Table 6: Lyapunov exponents ℓ_j and dimension D_L of the attractors in Fig. 22, computed using 10^7 iterates of the derivative.

	ρ_1	σ_{ρ_1}	ρ_2	σ_{ρ_2}	ρ	σ_ρ
A	0.057742563	1.7e-09	-0.449590703	2.3e-09	-0.128433623	6.4e-10
B	0.057857519	1.4e-09	-0.43952775	2.6e-08	-0.131635645	8.7e-10
C	0.057985171	1.1e-09	-0.434888784	5.1e-10	-0.133333333	4.7e-10
D	0.05813534	7.4e-08	-0.4299	1.3e-04	-0.135237	7.3e-06

Table 7: Rotation numbers ρ_j and uncertainties σ_{ρ_j}, for $j = 1, 2$, together with ratio $\rho = \rho_1/\rho_2$ and related uncertainty $\sigma_\rho = \rho_2\sigma_{\rho_1} + \rho_1\sigma_{\rho_2} + \sigma_{\rho_1}\sigma_{\rho_2}$, for the attractors in Fig. 22, computed using 10^6 iterates of G along an orbit.

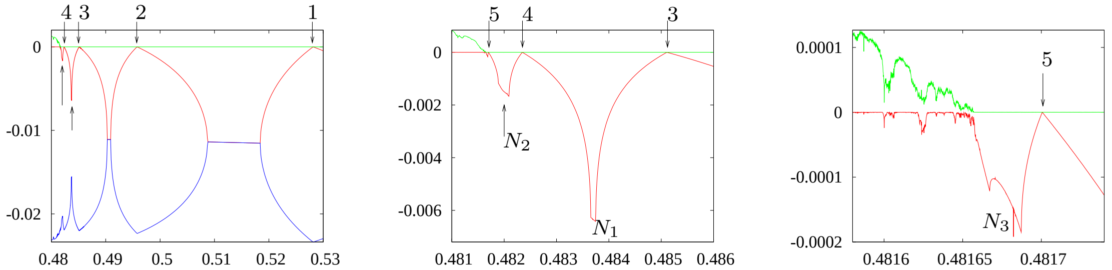

Figure 21: Left: Lyapunov exponents $\ell_1 \geq \ell_2 \geq \ell_3$ (in green, red, and blue, respectively), for $\delta/(2\pi)$ fixed at 0.0324 and for a decreasing sequence of values of μ. Centre, right: subsequent magnifications near the formation of a quasi-periodic strange attractor. Locations of quasi-periodic period doublings are labelled by 1 to 5. Parameter values for which non-reducibility of the attracting invariant circle occurs are labelled by N_1, N_2, N_3 (centre and right panels). N_1 and N_2 are marked by arrows in the left panel.

same situation as in Fig. 9). The ratio $\rho = \rho_1/\rho_2$ of the two rotation numbers on $\mathscr{T}_-$ is displayed in Fig. 23 (a): as the resonance tongue is approached, ρ converges with a square-root asymptotics to the value assumed inside the tongue. Higher-order resonances are detected nearby, forming *plateaus* of constant ρ. For parameters in the plateaus, the two-torus is phase-locked to an invariant circle and the second Lyapunov exponent ℓ_2 is negative (see the box in Fig. 23 (c)).

The dynamics takes place on the attracting invariant circle $\mathscr{L}_-$ (as in Fig. 22 C) for parameters in the largest plateau in Fig. 23 (a). Inside this resonance tongue, $\mathscr{L}_-$ turns to focus type in the parameter interval where the Lyapunov exponents ℓ_2 and ℓ_3 are equal (Fig. 23 (c)). We conjecture that the resonant two-torus is destroyed by a homoclinic tangency of the manifolds $W^s(\mathscr{L}_+)$ and $W^u(\mathscr{L}_+)$, taking place somewhere inside this resonance tongue. When $\mathscr{L}_-$ disappears by collapsing with $\mathscr{L}_+$ (across the leftmost extreme of the tongue), a strange attractor shows up (Fig. 22 D), having a positive Lyapunov exponent (Fig. 23 (c)). A slice of this attractor by a thin 'equatorial' layer displays a folded curve structure in the transversal direction (Fig. 24). Slices of the attractors in Fig. 20 D display a similar structure.

Remarkably, a regular pattern of resonance tongues persists also in the chaotic region after the breakdown of the two-torus. Many intervals are detected where the first Lyapunov exponent ℓ_1 is zero, see Fig. 23 (d). Computation of the rotation vector (ρ_1, ρ_2) confirms that these intervals are resonance tongues where the strange attractor is phase-locked to an attracting invariant circle (Fig. 23 (c)). This pattern is reminiscent of the distribution of periodic windows (parameter intervals where the dynamics is characterised by sinks) amid the chaotic range in the logistic map [38].

Remark 3. There are striking analogies in the tongue-like structure displayed in Fig. 19 and that described in [15] for a map M of the cylinder $\mathbb{R}\times\mathbb{S}^1$. The 'fattened Arnol′d map' M is constructed as an approximate return map near a homoclinic tangency of a fixed point of saddle type. Heuristically speaking, the map G can be seen as a perturbation of the fattened Arnol′d map M where the role of the homoclinic tangency is played by a heteroclinic tangency of the two fixed points of saddle-focus type. A study of the relationship between the maps G and M is in preparation.

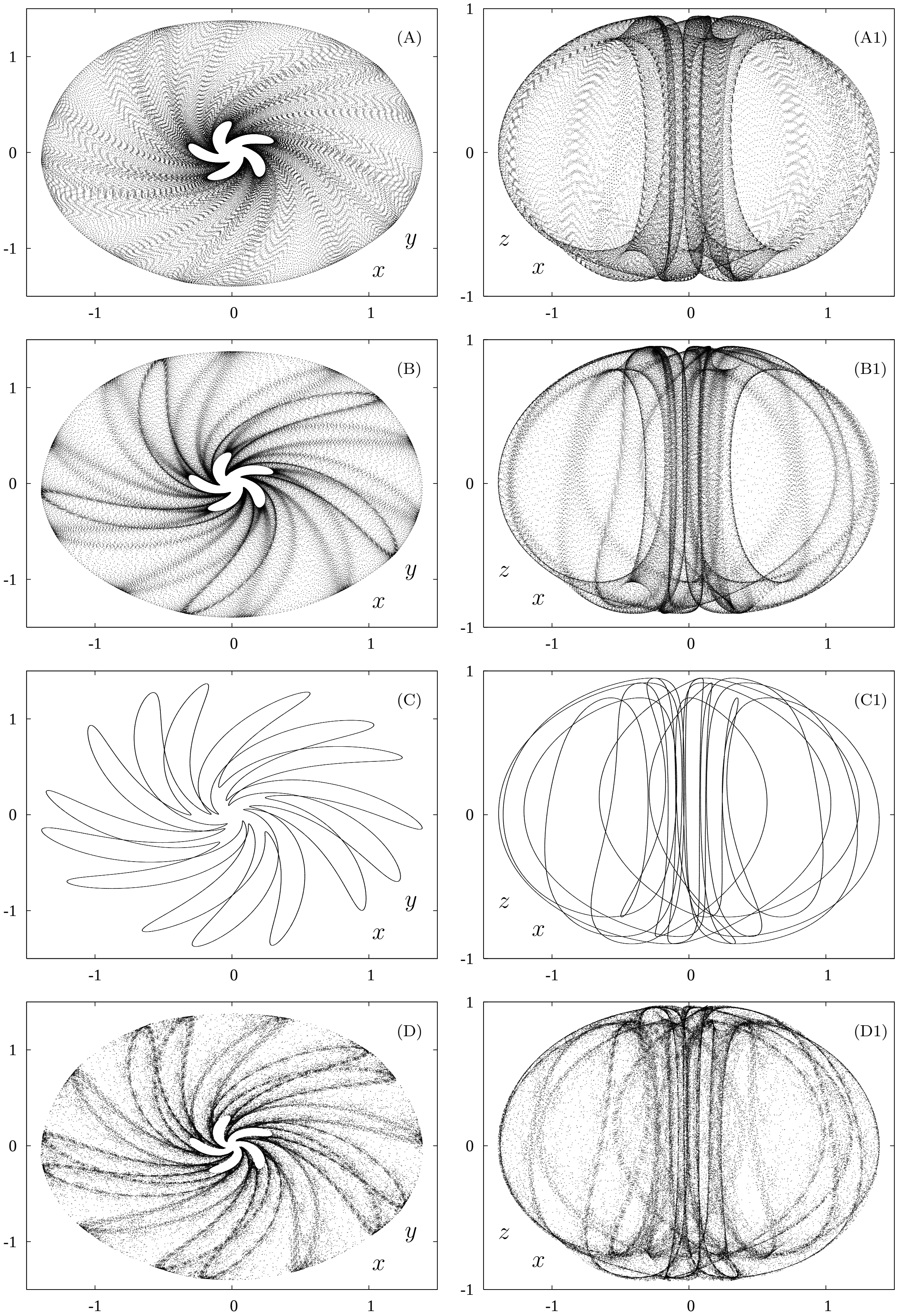

Figure 22: Attractors of the model map G (3) for $\delta/(2\pi) = 0.0247$ fixed and four values of μ. Projections on (x, y) (left column), where $w = x + iy$ and on (x, z) (right column). (A) $\mu = 0.47$, (B) 0.466, (C) 0.46, (D) 0.4555, see Tab. 6 for the Lyapunov exponents and Tab. 7 for the rotation numbers.

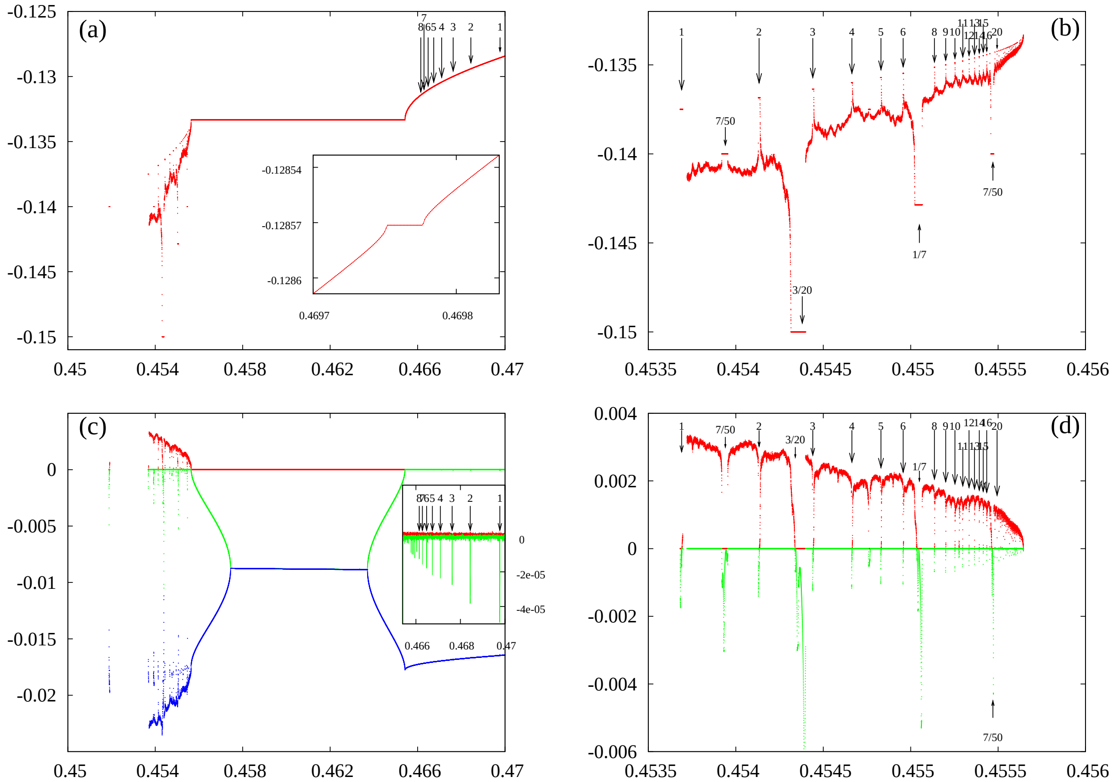

Figure 23: (a) Ratio $r = \rho_1/\rho_2$ of the rotation numbers of the two-torus $\mathscr{T}_-$ as a function of μ. For μ-values where the two-torus does not exist, the algorithm is applied to the detected attractor of G. The large plateau of constant $r = 2/15$ identifies a 2:15 resonance tongue where $\mathscr{T}_-$ is phase-locked to an attracting periodically invariant circle. A sequence of higher order resonances on $\mathscr{T}_-$ is marked by arrows labelled by an integer j which denotes resonance $r = (9 + 2*(j-1))/(70 + 15*(j-1))$, for $j = 1$ to 8. The rightmost resonance $j = 1$ is magnified in the box. (b) A regular pattern of resonance plateaus exists in the chaotic region for μ at the left of the large 2:15 resonance plateau. The indices j denote resonances $r = (11 + 2*(j-1))/(80 + 15*(j-1))$, where j increases from 1 to 20 (with some missing values). (c) Lyapunov exponents $\ell_1 \geq \ell_2 \geq \ell_3$ (red, green, blue, respectively), same μ-window as (a). Narrow intervals where $\ell_1 = 0$ and $\ell_2 < 0$ (see the magnification in the box) correspond to the higher order resonances labelled in (a). (d) ℓ_1 (red) and ℓ_2 (green) for the same μ-values of (b). Intervals where $\ell_1 = 0$ and $\ell_2 < 0$ match with the resonances identified in (b).

4 Discussion

Our dynamical inventory shows that model map G displays all the basic phenomena to be expected in generic 3D HSN-families of diffeomorphisms, within the unfolding class chosen for the Poincaré-Takens normal form (4), see Fig. 1. This unfolding class is the dynamically richest for HSN vector fields [38, 50]. Several phenomena detected for G require further, specific investigation. For the 1:5 resonance bubble we propose the following list (see Sec. 2.2 for details):

1. to clarify the analogy between the structure of the 1:5 bubble of map G and the bifurcation diagram of the vector field of the cylinder examined in [48];

2. to characterise Bogdanov-Takens bifurcations of period five invariant circles;

3. to analyse the transition in Fig. 10 involving homoclinic tangencies of an invariant

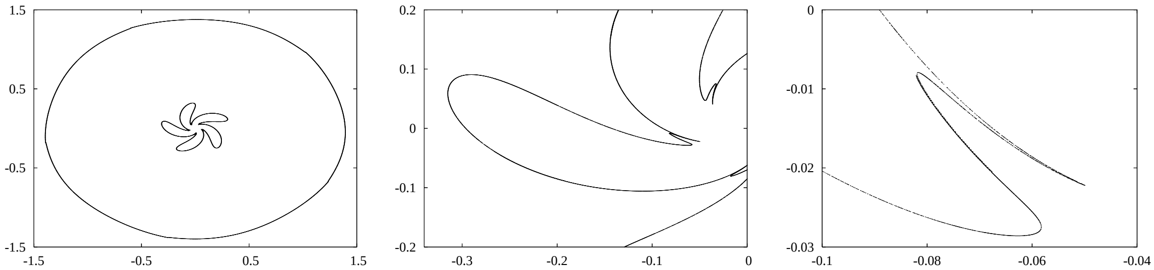

Figure 24: Left: a 'slice' of the attractor in Fig. 22 (D) is obtained by selecting points in a layer of width $2 \cdot 10^{-5}$ around the plane $z = 0$, projection on the (x, y)-plane. Centre: magnification of a portion of the section. Right: further magnification.

circle of focus type;

4. to study the transition in Fig. 11 involving the global repellor with five sphere-like heteroclinic structures (Fig. 12);

5. to determine whether the bifurcation structure of the 1:5 bubble is generic.

Moreover, it remains to be clarified what is the nature of the other resonance gaps individuated in Fig. 3 along the quasi-periodic Hopf boundary.

Open issues concerning the phenomena in region $\mathcal{HET}$ (Fig. 2 (b)) are:

1. the reason why Shil′nikov-like attractors are not detected near the homoclinic tangencies of the saddle-focus point P_- (see Sec. 3.1);

2. the analysis of the dynamics associated to Shil′nikov-like scenarios for 3D maps, at the light of the considerations made in Sec. 3.1;

3. to establish a relation between the interruption of torus doubling cascades and loss-of-reducibility scenarios in [39, 40] (Sec. 3.2.1);

4. same as previous point for the intermittency route involving a quasi-periodic SN of an invariant circle (Sec. 3.2.2);

5. the analogy of the tongue-structure in Fig. 19 and that of [15].

We plan to return to the above problems in future research.

Acknowledgements

The authors are indebted to Enric Castellà, Angel Jorba and Robert Roussarie for help and suggestions and thank the respective institutions for kind hospitality. RV acknowledges kind support by the Willis Research Network (www.willisresearchnetwork.com). The research of CS has been supported by grant MTM2006-05849/Consolider (Spain).

A Computational methods for invariant manifolds

We begin by discussing 1D manifolds of fixed points. The same algorithm can be used for periodic points with a suitable power of the map G. Let p be a hyperbolic fixed point of saddle type for G such that the derivative D_pG has eigenvalues λ_j, $j = 1, 2, 3$ with $\lambda_1 \in \mathbb{R}$. Consider $\lambda_1 > 1 > |\lambda_j|$, $j = 1, 2$. The inverse G^{-1} is used for $0 < \lambda_1 < 1 < |\lambda_j|$

and G^2 (or its inverse) for $\lambda_1 < 0$. The (local) unstable manifold of p is expressed as an adapted parametrisation

$$W : \mathbb{R} \to \mathbb{R}^3, \quad \text{with} \quad W(0) = p, \quad \text{such that} \quad G(W(t)) = W(\lambda_1 t). \tag{7}$$

The Taylor coefficients of W at the origin are computed with an algebraic manipulator up to a given order (typically 10 or 20), using the method in [60, Sec. 10]. A fundamental domain is computed as an interval of t where the representation as a truncated Taylor series is accurate. Specifically the fundamental domain is defined as the interval $(t_0/\lambda_1, t_0)$, where t_0 is such that

$$|G(W(t)) - W(\lambda_1 t))| < \varepsilon \tag{8}$$

and ε is a user-prescribed tolerance (typically $1.e-15$). The manifold is then 'globalised' as explained in [60, Sec. 11] (to which we refer for more details): three initial points $p_j = W(t_j)$, $j = 1, 2, 3$ are chosen with t_j in the fundamental domain. For $j = 2$ let $\Delta t_j = t_j - t_{j-1}$, $\Delta s_j = \|p_j - p_{j-1}\|$ and define $\Delta\alpha_j$ as the angle between the segments $\overline{p_j, p_{j-1}}$ and $\overline{p_{j-1}, p_{j-1}}$. A new point is computed by setting $p_{j+1} = W(t_{j+1})$, with $t_{j+1} = t_j + \Delta t_{j+1}$. If the new value t_{j+1} is larger than the upper extreme of the fundamental domain, then both t_{j+1} and Δt_{j+1} are divided by λ_1 and p_{j+1} is defined as $G(W(t_{j+1}))$: the iterate number is increased by one. This procedure is repeated, incrementing the iterate number every time that the parameter t_{j+1} exceeds t_0. If either Δs_j or $\Delta\alpha_j$ become too large (too small), then the step Δt_{j+1} is reduced. (resp. increased).

We now turn to the computation of the 2D manifolds. Consider first P_+ and denote a complex eigenvalue of the derivative $D_{P_+}G$ by $\lambda = a + ib$ (with $|\lambda| > 1$ and $a, b \in \mathbb{R}$). We look for an adapted parametrisation, that is a function $W : \mathbb{R}^2 \to \mathbb{R}^3$ such that

$$G(W(y_1, y_2)) = W(\Lambda(y_1, y_2)), \quad \text{where} \quad \Lambda(y_1, y_2) = \begin{pmatrix} a & -b \\ b & a \end{pmatrix} \begin{pmatrix} y_1 \\ y_2 \end{pmatrix}. \tag{9}$$

For simplicity, a linear approximation is used for $W^u(P_+)$:

$$W(y_1, y_2) = P_+ + y_1\mathbf{v} + y_2\mathbf{u}, \tag{10}$$

where $\mathbf{u}, \mathbf{v} \in \mathbb{R}^3$ are the real and imaginary parts of an eigenvector $\mathbf{w} = \mathbf{u} + i\mathbf{v}$ of $D_{P_+}G$ corresponding to the eigenvalue λ. Since Λ in (9) acts on $(y_1, y_2) \in \mathbb{R}^2$ as the complex multiplication λz, with $z = y_1 + iy_2 \in \mathbb{C}$, a fundamental domain is an annulus in the (y_1, y_2)-coordinates. Numerically, we look for $z^0 = y_1^0 + iy_1^0$ such that

$$\left|G(W(y_1^0, y_1^0)) - W(\lambda z^0))\right| < \varepsilon, \tag{11}$$

where the tolerance ε is fixed at $1.e - 15$. Then a fundamental domain is the annulus bounded by the circles with centre the origin and radii $|z^0|$ and $|z^0/\lambda|$.

The intersection of $W^u(P_+)$ with the plane $\{z = 0\}$ is computed as follows. A grid of points on the outer circle bounding the fundamental domain is iterated under G until the n-th image of this grid lies below the horizontal plane $\{z = 0\}$ and the $n-1$-th image lies above it. In certain cases, for the latter condition to be verified it is necessary to slightly shift the fundamental domain (this is done by reducing the modulus of z^0). The intersection with $\{z = 0\}$ is computed for each point on the grid by a secant method: this yields a mesh of points in the *first* intersection of $W^u(P_+)$ with $\{z = 0\}$. The first intersection of $W^s(P_-)$ with $\{z = 0\}$ is computed in the same way. The 'equatorial' heteroclinic tangencies between $W^u(P_+)$ and $W^s(P_-)$ are computed by looking for zeroes of the signed distance $sd(\theta)$ between the first intersections $W^u(P_+) \cap \{z = 0\}$ and $W^s(P_-) \cap \{z = 0\}$, see Sec. 3.1 for details.

The curves $I_{P_\pm}$ and $O_{P_\pm}$ of 'inner' and 'outer' Shil′nikov homoclinic tangencies (see Sec. 3.1) are computed as follows. Consider P_-: for fixed parameter values, a grid of points is selected inside a fundamental domain for $W^u(P_-)$ and a fixed number of iterates of G is computed for each of these points. Considering a fixed a neighbourhood N of the origin, there are three possibilities, corresponding to three open regions of the parameter plane: all iterates remain inside N, all iterates escape from N, or part of the iterates escapes and part remains inside N. These three situations correspond, respectively, to the left, right and centre panels of Fig. 16 (bottom row). For large μ, the first configuration occurs. The (μ, δ)-parameter plane is then scanned along horizontal line (that is, for fixed δ) and by decreasing μ each time, until the configuration changes: in this way, the μ-value of the 'inner' (first-return) Shil′nikov tangency is *bracketed.*

A bisection procedure is then started to locate the occurrence up to a specified precision (typically, 1.e-12). Here the more refined algorithm described at the beginning of this section is used for computation of $W^u(P_-)$. Near the first-return of $W^u(P_-)$ to a neighbourhood of P_-, the images of the fundamental domain develop oscillations (Fig. 16 bottom row): the trick is to focus on the minimum z-values of such oscillations. Near the 'inner' Shil′nikov tangency, during subsequent iterations of the fundamental domain the z-minima approach P_- spiralling around it and there are two possibilities: the minima may ultimately 'climb up again' or they may fall below $W^s(P_-)$. In the former case, we are still 'before' the tangency (Fig. 16 bottom left); in the latter case we are 'after' the tangency (Fig. 16 bottom left).

B Computation of quasi-periodic bifurcations

Quasi-periodic bifurcations of invariant circles are computed by numerical continuation and analysis of normal behaviour, both Fourier-based. We here follow [27, 28, 43], see [37, 51] for alternative methods. Let $f : \mathbb{R}^n \to \mathbb{R}^n$ be a diffeomorphism and let $\mathbb{T}^1 = \mathbb{R}/2\pi\mathbb{N}$ denote the unit circle. An invariant circle with rotation number ρ is represented by a parametrisation $x : \mathbb{T}^1 \to \mathbb{R}^n$ which satisfies the invariance equation

$$F(x) = 0, \quad \text{where} \quad F(x)(\theta) = f(x(\theta)) - x(\theta + \rho) \quad \text{for all } \theta \in \mathbb{T}^1. \tag{12}$$

Eq (12) defines a functional F on the space $\{x : \mathbb{T}^1 \to \mathbb{R}^n\}$ of continuous parametrisations. A truncation order N is fixed and x is discretised as a truncated Fourier series

$$x_N(\theta) = a_0 + \sum_{k=1}^{N} a_k \cos(k\theta) + b_k \sin(k\theta), \quad a_0, a_k, b_k \in \mathbb{R}^n. \tag{13}$$

The image of x_N under the functional F is evaluated at the $(2N + 1)$ mesh points $\theta_j = 2\pi j/(2N+1) \in \mathbb{T}^1$, $j = 0, \ldots, 2N$: this yields a function of the Fourier coefficients, defined by

$$F_N : \mathbb{R}^{(2N+1)n} \to \mathbb{R}^{(2N+1)n}, \quad (a_0, a_k, b_k)_{k=1}^N \mapsto (f(x_N(\theta_j)) - x_N(\theta_j + \rho))_{j=0}^{2N}. \tag{14}$$

A solution of the discretised functional equation $F_N((a_0, a_k, b_k)_{k=1}^N) = 0$ yields an approximation of the invariant circle $x(\theta)$, expressed as a truncated series $x_N(\theta)$ as in (13). Zeroes of eq. (14) are found by a Newton algorithm starting from approximate values for the Fourier coefficients $(a_0, a_k, b_k)_{k=1}^N$. The differential of F_N around an invariant circle has a one-dimensional kernel, due to the freedom in choosing the origin of θ. This can be dealt with in various ways: for example one can fix $b_1 = 0$ or fix the value of a component of one of the x_j's at $\theta = 0$. If the rotation number is not known exactly, a modified Newton algorithm can be used to refine initial approximations for both the Fourier coefficients and ρ [60]. If f depends on parameters $p_1, \dots, p_m$ and if the parameter values for which the circle exists are only known approximately, then a modified Newton algorithm can be devised to refine initial approximations for $(a_0, a_k, b_k)_{k=1}^N$, ρ and $p_1, \dots, p_m$ simultaneously.

The normal behaviour of a quasi-periodic invariant circle is computed with the method of [43]. Given an invariant circle parametrised by $x(\theta)$, since

$$f(x(\theta) + h) = f(x(\theta)) + D_x f(x(\theta))h + O(||h||^2), \tag{15}$$

the linear normal behaviour around $x(\theta)$ is described by the skew-product system

$$(h, \theta) \mapsto (A(\theta)h, \theta + \rho), \tag{16}$$

where $A(\theta) = D_x f(x(\theta))$ and $h \in \mathbb{R}^n$. If the invariant circle is reducible [43], then the normal behaviour is fully characterised by the eigenvalues λ obtained from

$$(T_{-\rho} \circ A(\theta))\psi(\theta) = \lambda\psi(\theta), \quad \text{where} \quad T_\rho\psi(\theta) = \psi(\theta + \rho) \tag{17}$$

defines a functional on the space $\{\psi : \mathbb{T}^1 \to \mathbb{C}^n\}$ of continuous parametrisations. The idea is to derive finite dimensional approximations for the operators $T_{-\rho}$ and $A(\theta)$. A discretised version A_N of A is given by the Jacobian of the mapping in (14). A discretisation of T_ρ is the block-diagonal matrix where each block is a 2×2 matrix corresponding to rotation of angle $k\rho$: indeed, the rotation $\theta \mapsto \theta + \rho$ applied to the Fourier series in (13) is a rotation of angle $k\rho$ on each subspace corresponding to (a_k, b_k). If the circle is reducible, then the eigenvalues of the discretised operator $(T_{-\rho} \circ A(\theta))_N$ provide approximations for $(\lambda^\parallel, \lambda_1^\perp, \lambda_2^\perp)$: here $\lambda_j^\perp, j = 1, 2$ correspond to the linear dynamics in the normal directions to the circle and $\lambda^\parallel = 1$ to the tangent linear dynamics.

By dissipative KAM theory [4, 7, 8, 32], an invariant circle $\mathscr{C}$ of G has irrational (Diophantine) rotation number on a Cantor-like foliation of curves in the (δ, μ)-parameter plane. The rotation number ρ is constant on each line in the foliation. The foliation has positive Lebesgue measure but is nowhere dense in the parameter plane: there exists an open and dense subset of resonance gaps such that for parameters inside a gap the circle $\mathscr{C}$ is phase-locked to periodic orbits and the rotation number is rational. This structure is illustrated in Fig. 25 for the invariant circles of the fifth iterate G^5 near the 1:5 bubble, see Sec. 2.2. The locus of (μ, δ)-values for which $\mathscr{C}_-^5$ has a fixed irrational (Diophantine) rotation number $\rho = \rho_0$ is found to be a closed loop for many rotation numbers. Several of these 'Diophantine loops' are plotted in Fig. 25 (a), together with the Hopf ellipse $\mathcal{SN}_\mp^5$ and the 1:5 gap boundaries $\mathcal{SN}_\pm^5$, compare with Fig. 7. Resonance gaps are detected among the lines of the Cantor-like foliation. A resonance gaps of order 50 is plotted in Fig. 25 (a) (in magenta). This gap is a narrow strip having the same shape as the Diophantine loops and it is bounded by two curves of saddle-node bifurcations of periodic points with period 50.

Suppose that we have a numerical approximation $x_N(\theta)$ of $\mathscr{C}_-^5$, with rotation number ρ, for parameter values (δ, μ). A strategy for the numerical continuation of $x_N(\theta)$ might be to 'move' δ and use a modified Newton method to refine x_N and ρ. A problem with this approach is that the new value of δ might fall inside a resonance gap: this causes numerical problems in the modified Newton method. Indeed, the truncation order N must be very high to get convergence: a phase-locked circle generically is finitely differentiable, meaning that its Fourier coefficients decay slowly. Keeping ρ fixed and 'moving' both (δ, μ) is numerically more stable. Each loop in Fig. 25 is computed in this way, by a predictor-corrector algorithm using pseudo-arclength [60]. The predictor step

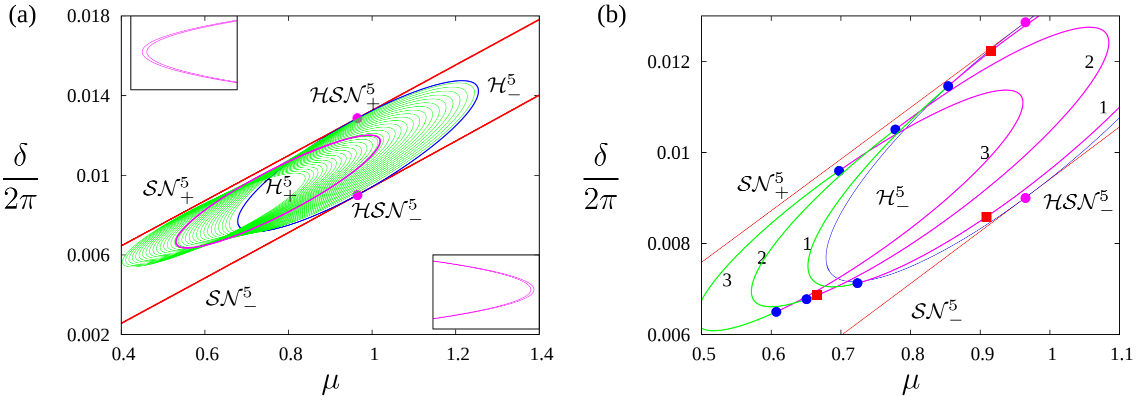

Figure 25: (a) The Hopf ellipse $\mathcal{H}^5_\pm$ (blue) and the boundaries $\mathcal{SN}^5_\pm$ (red) of the 1:5 resonance tongue are plotted together with several Diophantine loops (green) in the parameter plane, see text. The rotation number of the period five circle $\mathscr{C}^5_-$ varies of 0.0007 between adjacent loops. A resonance gap of order 50 is bounded by two curves of saddle-node bifurcations of period 50 periodic points (in magenta). The boxes contain magnifications of the resonance gap near its rightmost and leftmost parts. (b) Magnification of (a) showing only three loops. Red squares and blue dots mark bifurcations of $\mathscr{C}^5_-$: Hopf and saddle-node, respectively.

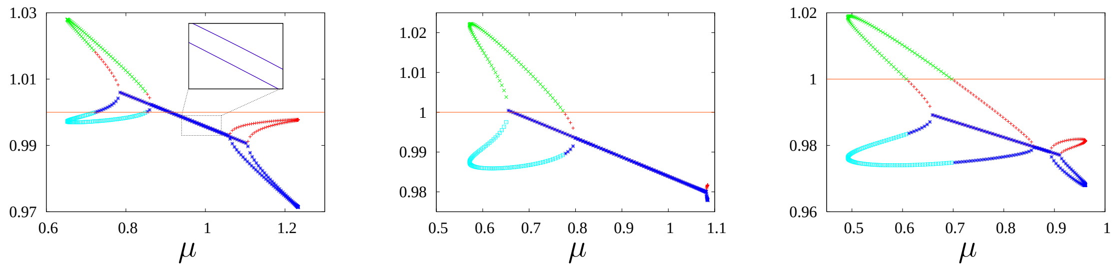

Figure 26: Left: modulus of the 'normal' eigenvalues $\lambda^\perp_{1,2}$ of $\mathscr{C}^5_-$ (red and blue) and of $\mathscr{C}^5_+$ (green and pale blue) as a function of μ along loop 1 (closest to $\mathcal{H}^5_\pm$) in Fig. 25 (b). The magnification in the box (slightly tilted for better visibility) shows that there is no overlapping where $\lambda^\perp_{1,2}$ are complex. Centre, right: same as left for loop 2 and 3, respectively (again, there is no overlapping). Branch switching from $\mathscr{C}^5_-$ to $\mathscr{C}^5_+$ occurs when $\lambda^\perp_{1,2} \in \mathbb{R}$ and one of them crosses the value 1, through a quasi-periodic saddle-node bifurcation belonging to $\mathcal{SNC}^5_-$ or $\mathcal{SNC}^5_+$.

is based on Lagrange extrapolation: this provides approximate values for the Fourier coefficients $(a_0, a_k, b_k)^N_{k=1}$ and for the new (δ, μ)-parameter values for which the rotation number remains unaltered. A modified Newton corrector with fixed ρ is used to refine $(a_0, a_k, b_k)^N_{k=1}$ and (δ, μ). Once a loop is computed, the value of ρ is changed by a small amount (preserving irrationality) and a new loop is computed. Truncation order as low as $N = 20$ is sufficient if ρ is Diophantine.

Quasi-periodic bifurcations are detected by monitoring the normal eigenvalues $\lambda^\perp_j, j = 1, 2$ during the numerical continuation of invariant circles. Quasi-periodic saddle-node bifurcations correspond to $\lambda^\perp_{1,2} \in \mathbb{R}$ and $\lambda^\perp_1 = 1$ or $\lambda^\perp_2 = 1$. Quasi-periodic saddle-node bifurcations correspond to $\lambda^\perp_1 = \overline{\lambda^\perp_2} \in \mathbb{C}$ and $|\lambda^\perp_1| = 1$. Fig. 25 (b) shows the location of quasi-periodic Hopf and saddle-node bifurcations of $\mathscr{C}^5_-$ along three loops with constant rotation number. In loop 1 (the closest to the Hopf ellipse $\mathcal{H}^5_\pm$) the Hopf and saddle-node bifurcations are distant from each other, whereas in loop 3 (the farthest from $\mathcal{H}^5_\pm$) no Hopf bifurcation occurs. In our notation, $\mathscr{C}^5_-$ might be either attracting or repelling, whereas $\mathscr{C}^5_+$ is always of saddle type. Numerical continuation along each loop switches from $\mathscr{C}^5_-$ to $\mathscr{C}^5_+$ (or viceversa) across the quasi-periodic saddle-node bifurcations: the two branches in each loop are plotted in different colours in Fig. 25 (b).

Fig. 26 shows the modulus $|\lambda^\perp_{1,2}|$ against the parameter μ along each of the three loops in Fig. 25 (b). For each fixed μ, four distinct values exist if the eigenvalues are real and two if they are complex. The intersection with the horizontal line $\left|\lambda^\perp_{1,2}\right| = 1$ identifies two saddle-node and two Hopf bifurcations in the left panel of Fig. 26. During the continuation with fixed rotation number, suitable test functions are monitored: if a test function changes sign, then the parameter value for which the bifurcation occurs is searched by a secant algorithm. The rotation number is kept fixed in the the secant algorithm: parameters are constrained to remain on the same Diophantine loop. The quasi-periodic bifurcation 'curves' $\mathcal{SNC}^5_-$ and $\mathcal{HC}^5_-$ in Fig. 7 are computed in this way: first a rotation number is fixed and the corresponding Diophantine loop is scanned searching for bifurcations. Then the rotation number is changed and the procedure is restarted. For example, the two squares in the lower branches of Fig. 25 (b) belong to $\mathcal{HC}^5_-$; the square in the upper branch belongs to $\mathcal{HC}^5_+$; the three blue dots in the lower branches belong to $\mathcal{SNC}^5_-$, the others to $\mathcal{SNC}^5_+$, compare with Fig. 8 (a).

References

[1] V.I. Arnol′d: *Geometrical Methods in the Theory of Ordinary Differential Equations (2nd ed.)*, Springer–Verlag (1988).

[2] C. Baesens, J. Guckenheimer, S. Kim, R.S. McKay: Three coupled oscillators: mode-locking, global bifurcations and toroidal chaos, *Phys. D* **49(3)** (1991), 387–475.

[3] M. Benedicks, L. Carleson: The dynamics of the Hénon map, *Ann. of Math. (2)* **133(1)** (1991), 73–169.

[4] B.L.J. Braaksma, H.W. Broer: On a quasi-periodic Hopf bifurcation, *Ann. Inst. H. Poincaré Anal. Non Linéaire* **4(2)** (1987), 115–168.

[5] H.W. Broer: Formal normal forms for vector fields and some consequences for bifurcations in the volume preserving case, in *Dynamical Systems and turbulence, Warwick 1980* (A. Dold and B. Eckmann Eds.), Springer LNM **898** (1980), 54–74.

[6] H.W. Broer, M. Golubitsky, G. Vegter: The geometry of resonance tongues: A Singularity Theory approach, *Nonlinearity* **16** (2003), 1511–1538.

[7] H.W. Broer, G.B. Huitema, M.B. Sevryuk: *Quasi-periodic Motions in Families of Dynamical Systems, Order amidst Chaos*, Springer LNM **1645** (1996).

[8] H.W. Broer, G.B. Huitema, F. Takens, B.L.J. Braaksma: Unfoldings and bifurcations of quasi-periodic tori, *Mem. AMS* **83(421)** (1990), 1–175.

[9] H.W. Broer, V. Naudot, R. Roussarie: Extension of catastrophe theory to Dulac unfoldings, in *Equadiff 2003, Proceedings International Conference on Differential Equations, Hasselt 2003*, (F. Dumortier, H.W. Broer, J. Mahwin and S.M. Verduyn-Lunel eds.), World Scientific, Singapore (2005), ISBN 981 256 169 2, 714–719.

[10] H.W. Broer, V. Naudot, R. Roussarie, K. Saleh and F.O.O. Wagener: Organising centres in the semi-global analysis of dynamical systems, *Int. J. Appl. Math. Stat.* **12** (2007), No. D07, 7–36.

[11] H.W. Broer, R. Roussarie: Exponential confinement of chaos in the bifurcation sets of real analytic diffeomorphisms, in *Global analysis of dynamical systems: Festschrift dedicated to Floris Takens for his 60th birthday* (H.W. Broer, B. Krauskopf, and G. Vegter Eds.), IOP Publish., Bristol (2001).

[12] H.W. Broer, R. Roussarie, C. Simó: On the Bogdanov-Takens bifurcation for planar diffeomorphisms, in *Equadiff 1991, Proceedings Western European Conference on Differential Equations, Barcelona 1991*, C. Perelló, C. Simó, J .Solà-Morales eds., World Scientific, London (1993), 81–92.

[13] H.W. Broer, R. Roussarie, C. Simó: Invariant circles in the Bogdanov-Takens bifurcation for diffeomorphisms, *ETDS* **16** (1996), 1147–1172.

[14] H.W. Broer, C. Simó: Hill's equation with quasi–periodic forcing: resonance tongues, instability pockets and global phenomena, *Bul. Soc. Bras. Mat.* **29** (1998), 253–293.

[15] H.W. Broer, C. Simó, J.C. Tatjer: Towards global models near homoclinic tangencies of dissipative diffeomorphisms, *Nonlinearity* **11** (1998), 667–770.

[16] H.W. Broer, C. Simó, R. Vitolo: Bifurcations and strange attractors in the Lorenz-84 climate model with seasonal forcing, *Nonlinearity* **15(4)** (2002), 1205–1267.

[17] H.W. Broer, C. Simó, R. Vitolo: Chaos and quasi-periodicity in diffeomorphisms of the solid torus, *preprint* `mp_arc` #05-107 (2005).

[18] H.W. Broer, C. Simó, R. Vitolo: The Hopf-Saddle-Node bifurcation for fixed points of 3D-diffeomorphisms: analysis of a resonance 'bubble', *Physica D* **237(13)** (2008), 1773–1799.

[19] H.W. Broer, C. Simó, R. Vitolo: The Hopf-Saddle-Node bifurcation for fixed points of 3D-diffeomorphisms: the Arnol′d resonance web, *Bull. Belgian Math. Soc. Simon Stevin* **15(5)** (2008), 769-787.

[20] H.W. Broer, C. Simó, R. Vitolo: Quasi-periodic Hénon-like attractors in the Lorenz-84 climate model with seasonal forcing, in *Equadiff 2003, Proceedings International Conference on Differential Equations, Hasselt 2003*, (F. Dumortier, H.W. Broer, J. Mahwin and S.M. Verduyn-Lunel eds.), World Scientific, Singapore (2005), ISBN 981 256 169 2, 714–719.

[21] H.W. Broer, F. Takens, F.O.O. Wagener: Integrable and non-integrable deformations of the skew Hopf bifurcation, *Regular and Chaotic Dynamics* **4(2)** (1999), 17–43.

[22] H.W. Broer, F. Takens: Formally symmetric normal forms and genericity, *Dynamics Reported* **2** (1989), 36–60.

[23] H.W. Broer, R. van Dijk, R. Vitolo: Survey of strong normal-internal $k : l$ resonances in quasi-periodically driven oscillators for $l = 1, 2, 3$, *Proceedings SPT 2007*, World Sci. Publ., Hackensack, NJ (2008), 45-55.

[24] H.W. Broer, S.J. van Strien: Infinitely many moduli of strong stability in divergence free unfoldings of singularities of vector fields, in *Geometric Dynamics, Proceedings, Rio de Janeiro 1981* (J. Palis Ed.), Springer LNM **1007** (1983), 39–59.

[25] H.W. Broer, G. Vegter: Subordinate Shil′nikov bifurcations near some singularities of vector fields having low codimension, *ETDS* **4** (1984), 509–525.

[26] H.W. Broer, R. Vitolo: Dynamical systems modeling of low-frequency variability in low-order atmospheric models. *Discrete Contin. Dyn. Syst. Ser. B* **10(2-3)** (2008), 401–419.

[27] E. Castellà: Sobre la dinàmica prop dels punts de Lagrange del sistema Terra-Luna, PhD thesis (in Catalan), Univ. of Barcelona (2003).

[28] E. Castellà, À. Jorba: On the vertical families of two-dimensional tori near the triangular points of the Bicircular problem, *Celestial Mechanics* **76** (2000), 35–54.

[29] A. Chenciner: Bifurcations de points fixes elliptiques. I. Courbes invariantes, *Publ. Math. IHES* **61** (1985), 67–127.

[30] A. Chenciner: Bifurcations de points fixes elliptiques. II. Orbites périodiques et ensembles de Cantor invariants, *Invent. Math.* **80** (1985), 81–106.

[31] A. Chenciner: Bifurcations de points fixes elliptiques. III. Orbites périodiques de "petites" périodes et élimination résonante des couples de courbes invariantes, *Publ. Math. IHES* **66** (1987), 5–91.

[32] M.C. Ciocci, A. Litvak-Hinenzon, H.W. Broer: Survey on dissipative KAM theory including quasi-periodic bifurcation theory based on lectures by Henk Broer, In: J. Montaldi and T. Ratiu (eds.), *Geometric Mechanics and Symmetry: the Peyresq Lectures*, Lecture Notes Series **LMS306**, Cambridge University Press (2005), 303–355. ISBN-13 978-0-521-53957-9.

[33] S-N. Chow, C. Li, D. Wang: *Normal Forms and Bifurcation of Planar Vector Fields*, Cambridge University Press, New York (1994).

[34] F. Dumortier, S. Ibáñez, H. Kokubu, C. Simó: About the unfolding of a Hopf-zero singularity, in preparation (2007).

[35] N. Fenichel: Persistence and smoothness of invariant manifolds for flows, *Indiana Univ. Math. J.* **21** (1971/72), 193–226.

[36] P. Gaspard: Local birth of homoclinic chaos, *Phys. D* **62(1–4)** (1993), 94–122.

[37] G. Gomez, J.M. Mondelo, C. Simó: Refined Fourier Analysis Procedures, *preprint Universitat de Barcelona* (2001).

[38] J. Guckenheimer, P. Holmes: *Nonlinear Oscillations, Dynamical Systems, and Bifurcations of Vector Fields*, Springer–Verlag (1983).

[39] À. Haro, R. de la Llave: Manifolds at the verge of a hyperbolicity breakdown, *Chaos* **16(1)** (2006), 013120.

[40] À. Haro, R. de la Llave: A Parameterization Method for the Computation of Invariant Tori and Their Whiskers in Quasi-Periodic Maps: Explorations and Mechanisms for the Breakdown of Hyperbolicity, *SIAM J. Appl. Dyn. Syst.* **6(1)** (2007), 142–207.

[41] M.W. Hirsch, C.C. Pugh, M. Shub: *Invariant Manifolds*, Springer LNM **583** (1977).

[42] G. Iooss, J.E. Los: Quasi-genericity of bifurcations to high-dimensional invariant tori for maps, *Comm. Math. Phys.* **119** (1988), 453–500.

[43] À. Jorba: Numerical computation of the normal behaviour of invariant curves of n-dimensional maps, *Nonlinearity* **14** (2001), 943–976.

[44] À. Jorba, J.C. Tatjer: A mechanism for the fractalization of invariant curves in quasi-periodically forced 1-D maps. *Discrete Contin. Dyn. Syst. Ser. B* **10(2-3)** (2008), 537–567.

[45] V. Kirk: Breaking of symmetry in the saddle-node Hopf bifurcation, *Phys. Lett. A* **154** (1991), 243–248.

[46] B. Krauskopf: Bifurcation sequences at 1:4 resonance: an inventory, *Nonlinearity* **7(3)** (1994), 1073–1091.

[47] B. Krauskopf, C. Rousseau: Codimension-three unfoldings of reflectionally symmetric planar vector fields, *Nonlinearity* **10** (1997), 1115–1150.

[48] B. Krauskopf, B. Oldeman: A planar model system for the saddlenode Hopf bifurcation with global reinjection *Nonlinearity* **17** (2004), 1119-1151.

[49] Yu. Kuznetsov, H.G.E. Meijer: Remarks on interacting Neimark-Sacker bifurcations, *Journal of Difference Equations and Applications* **12(10)** (2006), 1009–1035.

[50] Yu. Kuznetsov: *Elements of Applied Bifurcation Theory* (2nd ed.), Springer–Verlag (1998).

[51] J.M. Mondelo: *Contribution to the Study of Fourier Methods for Quasi-Periodic Functions and the Vicinity of the Collinear Libration Points*, PhD thesis, Universitat de Barcelona (2001).

[52] L. Mora, M. Viana: Abundance of strange attractors, *Acta Math* **171** (1993), 1–71.

[53] A.I. Neishtadt: The separation of motions in systems with rapidly rotating phase, *Prikladnaja Matematika i Mekhanika* **48** (1984), 133–139.

[54] S. Newhouse, J. Palis, F. Takens: Bifurcations and stability of families of diffeomorphisms, *Publ. Math. IHES* **57** (1983), 5–71.

[55] S. Newhouse, D. Ruelle, F. Takens: Occurrence of strange Axiom A attractors near quasiperiodic flows on $\mathbb{T}^m$, $m \geq 3$, *Comm. Math. Phys.* **64** (1978), 35–40.

[56] J. Palis, F. Takens: *Hyperbolicity & Sensitive Chaotic Dynamics at Homoclinic Bifurcations*, Cambridge Studies in Advanced Mathematics **35**, Cambridge University Press (1993).

[57] D. Ruelle, F. Takens: On the nature of turbulence, *Comm. Math. Phys.* **20** (1971), 167–192.

[58] K. Saleh and F.O.O. Wagener: Semi-global analysis of periodic and quasi-periodic $k : 1$ and $k : 2$ resonances, *preprint Univ. Amsterdam* (2006), available at `http://www1.fee.uva.nl/cendef/publications/`.

[59] C. Simó: On the Hénon–Pomeau attractor, *J.Stat.Phys.* **21** (1979), 465–494.

[60] C. Simó: On the analytical and numerical computation of invariant manifolds, in *Modern Methods in Celestial Mechanics* (D. Benest and C. Froeschlé Eds.), ed. Frontières, Paris (1990), 285–330. Available also at `http://www.maia.ub.es/dsg/2004/`.

[61] C. Simó: On the use of Lyapunov exponents to detect global properties of the dynamics, in *Equadiff 2003, Proceedings International Conference on Differential Equations, Hasselt 2003*, (F. Dumortier, H.W. Broer, J. Mahwin and S.M. Verduyn-Lunel eds.), World Scientific, Singapore (2005), ISBN 981 256 169 2, 714–719.

[62] C. Simó, H.W. Broer, R. Roussarie: A numerical survey on the Takens-Bogdanov bifurcation for diffeomorphisms, *European Conference on Iteration Theory 89*, (C. Mira *et al.* eds.), World Scientific, Singapore (1992), 320–334.

[63] F. Takens: Forced oscillations and bifurcations, in *Applications of Global Analysis* **1** (1974), Communications of the Mathematical Institute Rijksuniversiteit Utrecht **3**, reprinted in *Global analysis of dynamical systems: Festschrift dedicated to Floris Takens for his 60th birthday* (H.W. Broer, B. Krauskopf, and G. Vegter Eds.), IOP Publish., Bristol (2001).

[64] F. Takens: Singularities of vector fields, *Publ. Math. IHES* **43** (1974), 47–100.

[65] F. Takens, F.O.O. Wagener: Resonances in skew and reducible quasi-periodic Hopf bifurcations, *Nonlinearity* **13(2)** (2000), 377–396.

[66] J.C. Tatjer: Three dimensional dissipative diffeomorphisms with homoclinic tangencies, *ETDS* **21(1)** (2001), 249–302.

[67] L. van Veen: The quasi-periodic doubling cascade in the transition to weak turbulence. *Phys. D*, **210(3-4)** (2005), 249–261.

[68] M. Viana: Strange attractors in higher dimensions, *Bol. Soc. Bras. Mat* **24** (1993), 13–62.

[69] R. Vitolo: *Bifurcations of attractors in 3D diffeomorphisms*, PhD thesis, University of Groningen (2003).

[70] F.O.O. Wagener: Semi-local analysis of the $k : 1$ and $k : 2$ resonances in quasi-periodically forced systems, in *Global analysis of dynamical systems. Festschrift dedicated to Floris Takens for his 60th birthday* (H.W. Broer, B. Krauskopf, G. Vegter eds.), IOP, Bristol and Philadelphia (2001), 113–129

[71] F.O.O. Wagener: On the skew Hopf bifurcation, PhD Thesis, University of Groningen (1998).

[72] Q. Wang, L.-S. Young: Strange Attractors with One Direction of Instability, *Comm. Math. Phys.* **218** (2001), 1–97.